The Astrophysical Journal Letters, 949:L34 (21pp), 2023 June 1 https://doi.org/10.3847/2041-8213/acc94b

JWST Reveals a Possible $z \sim 11$ Galaxy Merger in Triply Lensed MACS0647–JD

Tiger Yu-Yang Hsiao[1], Dan Coe[1,2,3], Abdurro'uf[1,2], Lily Whitler[4], Intae Jung[2], Gourav Khullar[5], Ashish Kumar Meena[6], Pratika Dayal[7], Kirk S. S. Barrow[8], Lillian Santos-Olmsted[9], Adam Casselman[10], Eros Vanzella[11], Mario Nonino[12], Yolanda Jiménez-Teja[13,14], Masamune Oguri[15,16], Daniel P. Stark[4], Lukas J. Furtak[6], Adi Zitrin[6], Angela Adamo[17], Gabriel Brammer[18,19], Larry Bradley[2], Jose M. Diego[20], Erik Zackrisson[21], Steven L. Finkelstein[22], Rogier A. Windhorst[23], Rachana Bhatawdekar[24], Taylor A. Hutchison[25,56], Tom Broadhurst[26,27,28], Paola Dimauro[29], Felipe Andrade-Santos[30,31], Jan J. Eldridge[32], Ana Acebron[33,34], Roberto J. Avila[2], Matthew B. Bayliss[35], Alex Benítez[36], Christian Binggeli[21], Patricia Bolan[37], Maruša Bradač[37,38], Adam C. Carnall[39], Christopher J. Conselice[40], Megan Donahue[41], Brenda Frye[42], Seiji Fujimoto[18,19,22,57], Alaina Henry[1,2], Bethan L. James[2], Susan A. Kassin[1,2], Lisa Kewley[31], Rebecca L. Larson[22,58], Tod Lauer[43], David Law[2], Guillaume Mahler[44,45], Ramesh Mainali[25], Stephan McCandliss[1], David Nicholls[46,47], Norbert Pirzkal[2], Marc Postman[2], Jane R. Rigby[25], Russell Ryan[2], Peter Senchyna[48], Keren Sharon[49], Ikko Shimizu[50], Victoria Strait[18,19], Mengtao Tang[51], Michele Trenti[52,53], Anton Vikaeus[21], and Brian Welch[25,54,55]

[1] Center for Astrophysical Sciences, Department of Physics and Astronomy, The Johns Hopkins University, 3400 N Charles St. Baltimore, MD 21218, USA
yhsiao17@jhu.edu
[2] Space Telescope Science Institute (STScI), 3700 San Martin Drive, Baltimore, MD 21218, USA
[3] Association of Universities for Research in Astronomy (AURA), Inc. for the European Space Agency (ESA), USA
[4] Steward Observatory, University of Arizona, 933 N Cherry Ave, Tucson, AZ 85721, USA
[5] Department of Physics and Astronomy and PITT PACC, University of Pittsburgh, Pittsburgh, PA 15260, USA
[6] Physics Department, Ben-Gurion University of the Negev, P.O. Box 653, Be'er-Sheva 84105, Israel
[7] Kapteyn Astronomical Institute, University of Groningen, P.O. Box 800, 9700 AV Groningen, The Netherlands
[8] Department of Astronomy, University of Illinois at Urbana-Champaign, 1002 W Green St, Urbana, IL 61801, USA
[9] Kavli Institute for Particle Astrophysics and Cosmology, Stanford University, 452 Lomita Mall, Stanford, CA 94305-4085, USA
[10] Department of Aerospace Engineering, University of Illinois at Urbana, Champaign 104 S Wright St, Urbana, IL 61801, USA
[11] INAF—OAS, Osservatorio di Astrofisica e Scienza dello Spazio di Bologna, via Gobetti 93/3, I-40129 Bologna, Italy
[12] INAF-Trieste Astronomical Observatory, Via Bazzoni 2, I-34124, Trieste, Italy
[13] Instituto de Astrofísica de Andalucía, Glorieta de la Astronomía s/n, E-18008 Granada, Spain
[14] Observatório Nacional—MCTI (ON), Rua Gal. José Cristino 77, São Cristóvão, 20921-400, Rio de Janeiro, Brazil
[15] Center for Frontier Science, Chiba University, 1-33 Yayoi-cho, Inage-ku, Chiba 263-8522, Japan
[16] Department of Physics, Graduate School of Science, Chiba University, 1-33 Yayoi-Cho, Inage-Ku, Chiba 263-8522, Japan
[17] Department of Astronomy, Oskar Klein Centre, Stockholm University, AlbaNova University Centre, SE-106 91 Stockholm, Sweden
[18] Cosmic Dawn Center (DAWN), Copenhagen, Denmark
[19] Niels Bohr Institute, University of Copenhagen, Jagtvej 128, Copenhagen, Denmark
[20] Instituto de Física de Cantabria (CSIC-UC). Avda. Los Castros s/n. E-39005 Santander, Spain
[21] Observational Astrophysics, Department of Physics and Astronomy, Uppsala University, Box 516, SE-751 20 Uppsala, Sweden
[22] Department of Astronomy, The University of Texas at Austin, Austin, TX 78712, USA
[23] School of Earth and Space Exploration, Arizona State University, Tempe, AZ 85287-1404, USA
[24] European Space Agency, ESA/ESTEC, Keplerlaan 1, 2201 AZ Noordwijk, The Netherlands
[25] Observational Cosmology Lab, NASA Goddard Space Flight Center, Greenbelt, MD 20771, USA
[26] Department of Theoretical Physics, University of the Basque Country UPV/EHU, Bilbao, Spain
[27] Donostia International Physics Center (DIPC), E-20018 Donostia, Spain
[28] IKERBASQUE, Basque Foundation for Science, Bilbao, Spain
[29] INAF—Osservatorio Astronomico di Roma, via di Frascati 33, I-00078 Monte Porzio Catone, Italy
[30] Department of Liberal Arts and Sciences, Berklee College of Music, 7 Haviland Street, Boston, MA 02215, USA
[31] Center for Astrophysics, Harvard & Smithsonian, 60 Garden Street, Cambridge, MA 02138, USA
[32] Department of Physics, University of Auckland, Private Bag 92019, Auckland, New Zealand
[33] Dipartimento di Fisica, Università degli Studi di Milano, Via Celoria 16, I-20133 Milano, Italy
[34] INAF—IASF Milano, via A. Corti 12, I-20133 Milano, Italy
[35] Department of Physics, University of Cincinnati, Cincinnati, OH 45221, USA
[36] King's College London, University of London, Strand, London, WC2R 2LS, UK
[37] Department of Physics and Astronomy, University of California, Davis, 1 Shields Ave, Davis, CA 95616, USA
[38] Department of Mathematics and Physics, University of Ljubljana, Jadranska ulica 19, SI-1000 Ljubljana, Slovenia
[39] Institute for Astronomy, University of Edinburgh, Royal Observatory, Edinburgh, EH9 3HJ, UK
[40] Jodrell Bank Centre for Astrophysics, University of Manchester, Oxford Road, Manchester, M13 9PL, UK
[41] Physics & Astronomy Department, Michigan State University, East Lansing, MI 48824, USA
[42] Department of Astronomy, Steward Observatory, University of Arizona, 933 North Cherry Avenue, Tucson, AZ 85721, USA
[43] NSF's National Optical-Infrared Astronomy Research Laboratory, 950 North Cherry Avenue, Tucson, AZ 85719, USA
[44] Institute for Computational Cosmology, Durham University, South Road, Durham, DH1 3LE, UK
[45] Centre for Extragalactic Astronomy, Durham University, South Road, Durham, DH1 3LE, UK
[46] Research School of Astronomy and Astrophysics, Australian National University, Canberra, ACT 2611, Australia
[47] ARC Centre of Excellence for All Sky Astrophysics in 3 Dimensions (ASTRO 3D), Australia
[48] Carnegie Observatories, 813 Santa Barbara Street, Pasadena, CA 91101, USA
[49] Department of Astronomy, University of Michigan, 1085 S. University Ave, Ann Arbor, MI 48109, USA
[50] Department of Literature, Shikoku Gakuin University, 3-2-1 Bunkyocho, Zentsuji, Kagawa 765-8505, Japan
[51] Department of Physics and Astronomy, University College London, Gower Street, London, WC1E 6BT, UK
[52] School of Physics, University of Melbourne, Parkville, VIC 3010, Australia
[53] ARC Centre of Excellence for All-Sky Astrophysics in 3 Dimensions, University of Melbourne, Parkville, VIC 3010, Australia
[54] Department of Astronomy, University of Maryland, College Park, MD 20742, USA

[55] Center for Research and Exploration in Space Science and Technology, NASA/GSFC, Greenbelt, MD 20771, USA
Received 2023 January 18; revised 2023 March 23; accepted 2023 March 27; published 2023 June 2

Abstract

MACS0647–JD is a triply lensed $z \sim 11$ galaxy originally discovered with the Hubble Space Telescope. The three lensed images are magnified by factors of ∼8, 5, and 2 to AB mag 25.1, 25.6, and 26.6 at 3.5 μm. The brightest is over a magnitude brighter than other galaxies recently discovered at similar redshifts $z > 10$ with JWST. Here, we report new JWST imaging that clearly resolves MACS0647–JD as having two components that are either merging galaxies or stellar complexes within a single galaxy. The brighter larger component "A" is intrinsically very blue ($\beta \sim -2.6 \pm 0.1$), likely due to very recent star formation and no dust, and is spatially extended with an effective radius ∼70 ± 24 pc. The smaller component "B" ($r \sim 20^{+8}_{-5}$ pc) appears redder ($\beta \sim -2 \pm 0.2$), likely because it is older (100–200 Myr) with mild dust extinction ($A_V \sim 0.1$ mag). With an estimated stellar mass ratio of roughly 2:1 and physical projected separation ∼400 pc, we may be witnessing a galaxy merger 430 million years after the Big Bang. We identify galaxies with similar colors in a high-redshift simulation, finding their star formation histories to be dissimilar, which is also suggested by the spectral energy distribution fitting, suggesting they formed further apart. We also identify a candidate companion galaxy "C" ∼3 kpc away, likely destined to merge with A and B. Upcoming JWST Near Infrared Spectrograph observations planned for 2023 January will deliver spectroscopic redshifts and more physical properties for these tiny magnified distant galaxies observed in the early universe.

Unified Astronomy Thesaurus concepts: Galaxies (573); High-redshift galaxies (734); Strong gravitational lensing (1643); Galaxy clusters (584); Early universe (435)

1. Introduction

Galaxies have formed from the repeated mergers of small star-forming clumps over cosmic time, with some small galaxies left over even today, such as the Magellanic Clouds. JWST has now discovered two such small galaxies within the first 430 million years that are seen close to the very start of this process. Studies have shown that up to 85% of present-day massive galaxies went through a galaxy merger in their lifetime, indicating that galaxy mergers play an important role in the formation and evolution of galaxies (e.g., Bell et al. 2006; Stewart et al. 2009; Hopkins et al. 2010a; Lotz et al. 2011; Rodriguez-Gomez et al. 2015; Duncan et al. 2019; Sotillo-Ramos et al. 2022). The Milky Way itself likely experienced a major merger at $z \sim 2$ with the so-called Gaia-Sausage-Enceladus galaxy (Belokurov et al. 2018; Helmi et al. 2018; Bonaca et al. 2020; Naidu et al. 2021; Xiang & Rix 2022). Based on reconstructions of this event, Naidu et al. (2021) concluded that ≈50% of the stellar mass of the current halo of the Milky Way came from this galaxy. More generally speaking, mergers build up the stellar content and transform galaxy morphology (e.g., Toomre & Toomre 1972; Barnes 1992; Mihos & Hernquist 1996; Husko et al. 2023). Mergers are also believed to affect the kinematics and distribution of stars (e.g., Naab et al. 2009; van Dokkum et al. 2010; Newman et al. 2012), and play a key role in the growth of supermassive black holes (e.g., Treister et al. 2012; Ellison et al. 2019; Zhang et al. 2023).

JWST (Gardner et al. 2006) is a state-of-the-art infrared space-based telescope, which was launched in 2021 December and started scientific observations recently in 2022 July (Rigby et al. 2022). Numerous high-redshift candidates have been discovered based on their photometric redshifts and dropout selections (e.g., Adams et al. 2022; Atek et al. 2022; Bradley et al. 2022; Castellano et al. 2022; Donnan et al. 2023; Finkelstein et al. 2022; Harikane et al. 2023; Naidu et al. 2022; Whitler et al. 2022a; Yan et al. 2023). Within its first few months, JWST is quickly transforming our understanding of the early universe (e.g., with flat/disky galaxies reported at $z \sim 2$–6; Ferreira et al. 2022; Nelson et al. 2022).

Gravitational lensing by massive galaxy clusters magnifies the light and sizes of distant objects. Thanks to these cosmic telescopes, not only are the fluxes of faint objects in the early universe boosted to the observable regime, the sizes of small-scale structures are amplified (e.g., Claeyssens et al. 2023; Meštrić et al. 2022; Vanzella et al. 2022; Welch et al. 2023, 2022). Thus, lensing has enabled us to discover early galaxies and study their properties (e.g., Coe et al. 2013). In order to study several key scientific topics in the early universe, several lensing cluster surveys have been conducted, including the Cluster Lensing and Supernova survey with Hubble (CLASH;[59] Postman et al. 2012a), the Hubble Frontier Fields (Lotz et al. 2017), and the Reionization Lensing Cluster Survey[60] (Coe et al. 2019).

CLASH is one of the large Hubble treasury programs which adopted the lensing technique to study distant galaxies (e.g., Zheng et al. 2012; Coe et al. 2013; Bouwens et al. 2014; Bradley et al. 2014; Smit et al. 2014), supernovae and cosmology (e.g., Graur et al. 2014; Patel et al. 2014; Rodney et al. 2014; Strolger et al. 2015; Gómez-Valent & Amendola 2018; Riess et al. 2018), dark matter in clusters (e.g., Eichner et al. 2013; Pacucci et al. 2013; Sartoris et al. 2014; Umetsu et al. 2014; Merten et al. 2015), and galaxies in clusters (e.g., Postman et al. 2012b; Burke et al. 2015; Donahue et al. 2015; Connor et al. 2017; Fogarty et al. 2017).

CLASH imaged 25 massive galaxy clusters in 16 filters with the Hubble Space Telescope (HST) from the near-UV (∼200 nm) to near-IR (∼1.6 μm). Five of the clusters were selected for their strong lensing strength, including MACSJ0647.7+7015

[56] NASA Postdoctoral Fellow.
[57] Hubble Fellow.
[58] NSF Graduate Fellow.

[59] https://www.stsci.edu/~postman/CLASH/
[60] https://relics.stsci.edu

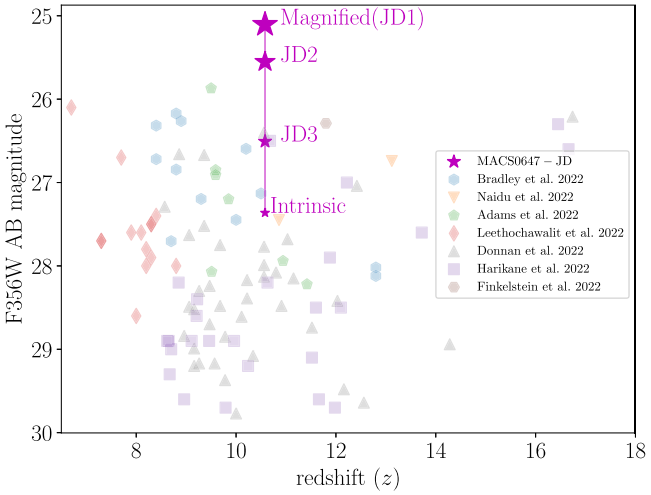

Figure 1. F356W AB magnitude vs. redshift for MACS0647–JD and $z \sim 8$–16 candidates recently discovered in JWST imaging (Adams et al. 2022; Bradley et al. 2022; Donnan et al. 2023; Finkelstein et al. 2022; Harikane et al. 2023; Leethochawalit et al. 2023; Naidu et al. 2022). MACS0647–JD is shown both as observed (magnified) and delensed (intrinsic) according to our models.

(MACS0647, $z = 0.591$; Ebeling et al. 2007) modeled by Zitrin et al. (2011). CLASH observations of MACSJ0647.7+7015 revealed 32 lensed $z \sim 6$–8 candidates (Bradley et al. 2014) and a triply lensed $z \sim 11$ candidate, MACS0647–JD (Coe et al. 2013).

MACS0647–JD had a photometric redshift $z = 10.7^{+0.6}_{-0.4}$ based on HST images, where it was detected in only the two reddest filters, F140W and F160W, dropping out of 15 bluer filters, including the J F125W, hence the name JD (J-band dropout). Despite lensing magnifications up to a factor of 8, MACS0647–JD was spatially unresolved in HST imaging.

MACS0647–JD was the first robust $z \sim 11$ candidate of the HST era, followed by GN-z11, which surpassed it at $z = 11.1$ (Oesch et al. 2016) and is similarly bright (F160W AB mag ~26) without the benefit of lensing magnification. Lensed as brightly as F356W AB mag 25.1, MACS0647–JD is 1–5 mag brighter than recently discovered $z \sim 8$–16 candidates reported in JWST imaging (Figure 1; Adams et al. 2022; Atek et al. 2023; Bradley et al. 2022; Donnan et al. 2023; Finkelstein et al. 2022; Harikane et al. 2023; Leethochawalit et al. 2023; Naidu et al. 2022). Because it is so bright, we can study its physical properties in more detail. More detail about the photometry measurement and the lensing will be later described in Sections 2 and 3.1.

Pirzkal et al. (2015) analyzed HST Wide Field Camera 3 (WFC3)/IR G141 grism spectroscopy of MACS0647–JD, concluding that any emission line bright enough to reproduce the observed photometry was ruled out by the observations. Any line or combination of emission lines with a flux of 10^{-17} erg s^{-1} cm^{-2} Å^{-1} would have been detected at the 5σ level, adding further support for $z \sim 11$, excluding a lower-redshift interloper, as in Brammer et al. (2013).

Lens modeling contributes geometric redshift corroboration based on the measured separations between the lensed images. The models in Coe et al. (2013) and Chan et al. (2017) both supported $z \sim 11$.

Lam et al. (2019) analyzed deep Spitzer imaging (50 hr band^{-1}), modeling and subtracting light of nearby galaxies to arrive at tentative detections of MACS0647–JD. Photometry varied between the three lensed images, yielding estimates of stellar mass $M_*/M_\odot \sim 10^8$–10^9, specific star formation rates (sSFRs) ~3–10 Gyr^{-1}, and ages ranging between ~10 and 400 Myr (the age of the universe at $z \sim 11$).

JWST observing program GO 1433 (PI: Coe) aims at studying MACS0647–JD in more detail, obtaining higher-resolution images, measuring colors, and obtaining spectroscopy to more precisely measure the redshift and constrain other physical properties including metallicity. Near Infrared Camera (NIRCam) imaging was obtained in six filters spanning 1.0–5.0 μm out to a ~4300 Å rest frame at $z = 10.6$. The second epoch of observations, planned for 2023 January, will obtain Near Infrared Spectrograph (NIRSpec) micro-shutter assembly (MSA) PRISM observations and add the NIRCam F480M filter, fully redward of the Balmer break, to obtain better measurements of ages and stellar masses at $z \sim 11$. All data from this program are public. We are releasing high-level science products and analysis tools online.[61]

In this paper, we report new observations of MACS0647–JD with six JWST NIRCam filters and derive physical properties including the stellar mass and dust content, while constraining the star formation history (SFH). This paper is organized as follows. In Section 2, we describe the JWST and HST observational data and the data-reduction process. In Section 3, we present the detected objects and their sizes and separations based on lens modeling. We detail photometry measurements in Section 4 and spectral energy distribution (SED) fitting in Section 5. In Section 6, we discuss our results, including measurements of physical parameters from SED fitting. We also present properties of analog galaxies identified with similar colors in a hydrodynamic simulation. We summarize our conclusions in Section 7.

We adopt the AB magnitude system ($m_{\rm AB} = 31.4 - 2.5\log(f_\nu/{\rm nJy})$; Oke 1974; Oke & Gunn 1983) and the Planck 2018 flat Lambda cold dark matter cosmology (Planck Collaboration et al. 2020) with $H_0 = 67.7$ km s^{-1} Mpc^{-1}, $\Omega_{\rm M} = 0.31$, and $\Omega_\Lambda = 0.69$, for which the universe is 13.8 billion years old, and $1'' \sim 4$ kpc at $z \sim 11$.

2. Observational Data

We analyze new JWST NIRCam images (GO 1433; PI: Coe), shown in Figure 2, as well as archival HST images, described below and detailed in Table 1. All of the data are publicly available in the Mikulski Archive for Space Telescopes (MAST; doi:10.17909/d2er-wq71). We also provide reduced data products aligned to a common pixel grid (Section 2.3).

2.1. Hubble Space Telescope Observations

MACS0647+70 has been observed with 39 orbits of HST imaging in 17 filters. It was first observed by programs GO 9722 (PI: Ebeling) and GO 10493 and 10793 (PI: Gal-Yam) in the Advanced Camera for Surveys (ACS) F555W and F814W filters. Then CLASH (GO 12101; PI: Postman) obtained imaging in 15 additional filters with WFC3/UVIS, ACS, and WFC3/IR, spanning 0.2–1.7 μm. Additional imaging in WFC3/IR F140W was obtained as part of a grism spectroscopy program (GO 13317; PI: Coe).

[61] https://cosmic-spring.github.io

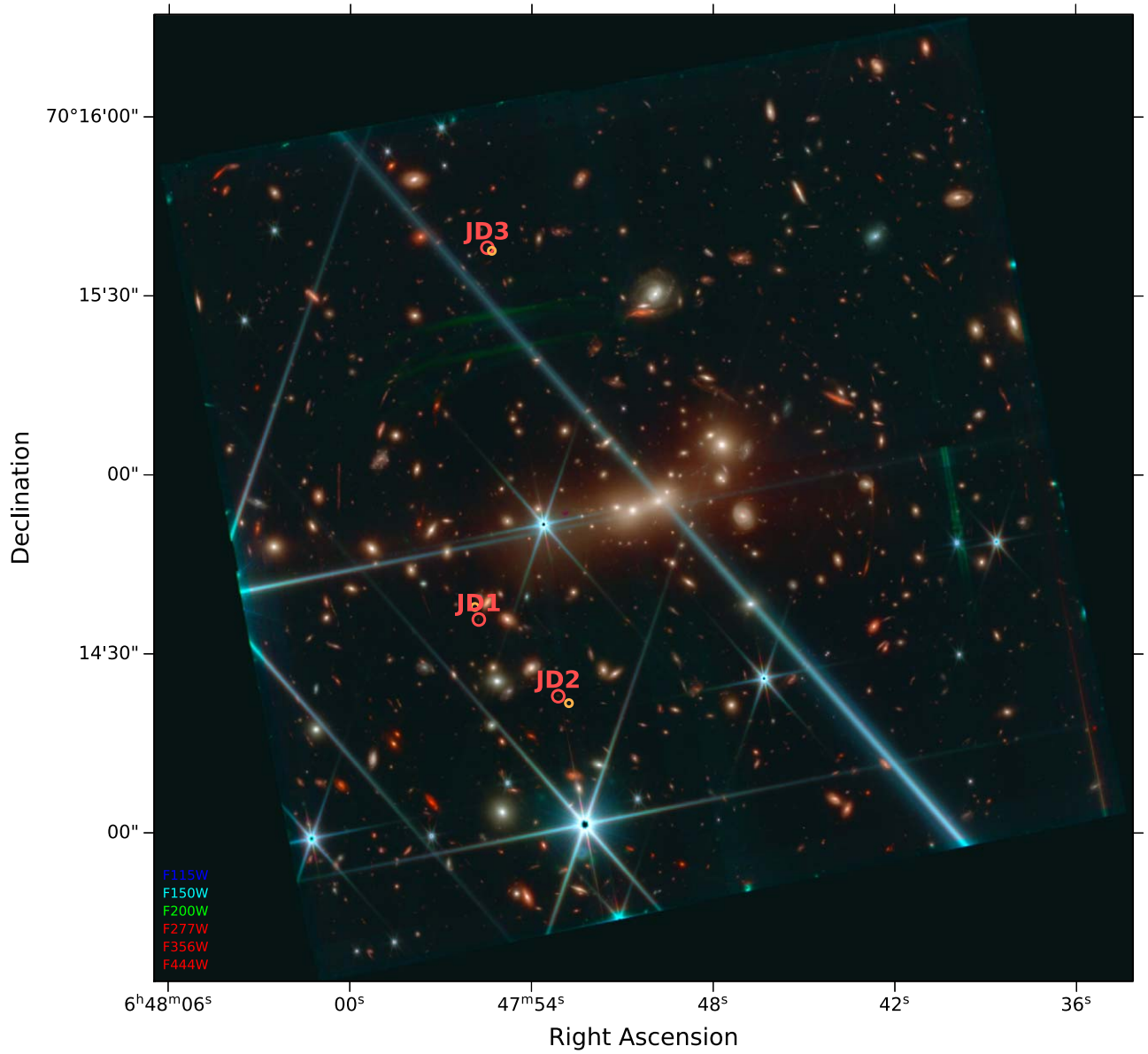

Figure 2. JWST NIRCam color image of MACS0647+70 with the three lensed images of MACS0647–JD labeled in red. Also circled in orange are the lensed images of a candidate companion galaxy C.

2.2. James Webb Space Telescope Observations

Here, we present new JWST NIRCam imaging in six filters, F115W, F150W, F200W, F277W, F365W, and F444W, spanning 1–5 μm. These public data were obtained on 2022 September 23 as part of Cycle 1 program GO 1433 (PI: Coe). Total exposure times of 2104 s in each filter achieved 5σ depths of AB mag 28.0 to 29.0 for small sources ($r = 0\farcs1$ aperture). Depths were measured by placing circular apertures in blank regions of the image using the PHOTUTILS `ImageDepth` routine.[62]

In each filter, we obtained four dithered exposures using INTRAMODULEBOX primary dithers to cover the 4″–5″ gaps between the short-wavelength detectors, while maximizing image area observed at full depth. Dithering also mitigates bad pixels and image artifacts, while improving resolution of the final drizzled images. Each exposure uses the SHALLOW4 readout pattern with 10 groups and one integration.

Backgrounds were relatively high that time of year for this target (∼80% higher than minimum). The telescope was rolled to a position angle of 280°. We observed the cluster in NIRCam module A and a nearby "blank" field with module B. The brighter lensed images, MACS0647–JD1 and JD2, were observed with NIRCam short-wavelength (SW) detector A3, while JD3 was observed with A1.

This program, GO 1433, will obtain additional public data, expected in 2023 January, consisting of NIRCam imaging in F200W and F480M and NIRSpec MSA PRISM spectroscopic observations.

2.3. Data Reduction

We process imaging data from MAST from all the programs above. The reduced images, along with source catalogs, are

[62] https://photutils.readthedocs.io/en/stable/api/photutils.utils.ImageDepth.html

Table 1
HST and JWST Exposure Times and Depths

Camera	Filter	λ (μm)	Exp. Time (s)	Depth[a] (AB)
HST WFC3/UVIS	F275W	0.23–0.31	3879	27.4
HST WFC3/UVIS	F336W	0.30–0.37	2498	27.6
HST WFC3/UVIS	F390W	0.33–0.45	2545	28.1
HST ACS/WFC	F435W	0.36–0.49	2124	28.0
HST ACS/WFC	F475W	0.39–0.56	2248	28.2
HST ACS/WFC	F555W	0.46–0.62	7740	28.7
HST ACS/WFC	F606W	0.46–0.72	2064	28.3
HST ACS/WFC	F625W	0.54–0.71	2131	27.9
HST ACS/WFC	F775W	0.68–0.86	2162	27.8
HST ACS/WFC	F814W[b]	0.69–0.96	8800	28.5
HST ACS/WFC	F850LP	0.80–1.09	4325	27.3
HST WFC3/IR	F105W	0.89–1.21	2914	28.3
HST WFC3/IR	F110W	0.88–1.41	1606	28.7
HST WFC3/IR	F125W	1.08–1.41	2614	28.3
HST WFC3/IR	F140W	1.19–1.61	2411	28.7
HST WFC3/IR	F160W	1.39–1.70	5229	28.4
JWST NIRCam	F115W	1.0–1.3	2104	28.1
JWST NIRCam	F150W	1.3–1.7	2104	28.3
JWST NIRCam	F200W	1.7–2.2	2104	28.4
JWST NIRCam	F277W	2.4–3.1	2104	28.9
JWST NIRCam	F356W	3.1–4.0	2104	29.0
JWST NIRCam	F444W	3.8–5.0	2104	28.8

Notes.
[a] 5σ point-source AB magnitude limit (within a $0\farcs2$ diameter aperture).
[b] We excluded one data set (J8QU04020: 3960 s) because it is contaminated by scattered light from the WFPC2 internal lamp, which was in use for a parallel program.

publicly available online along with public data from other JWST programs.[63]

We retrieve the individual calibrated exposures processed by the HST and JWST pipelines (`FLT` and Level 2b `CAL` images, respectively). We then process all of these using the GRIZLI pipeline (Brammer et al. 2022), coadding all exposures in each filter, and aligning all stacked images to a common $0\farcs04$ pixel grid with coordinates registered to the Gaia Data Release 3 (DR3) catalogs (Gaia Collaboration et al. 2021). The NIRCam short-wavelength images are drizzled to $0\farcs02$ pixels (on the same pixel grid supersampled $2\times$) to provide the highest possible resolution. We leave out the bluest filter HST WFC3/UVIS F225W image, which contains very few sources, making it difficult to process.

We make use of the latest NIRCam calibrations `jwst_0995.pmap`, based on data from NIRCam CAL program data and made operational 2022 October 6. These were not available at the time of processing, so we recalibrate our data in several steps. The JWST pipeline used NIRCam calibrations first made available July 29 in `jwst_0942.pmap`; these were the first photometric calibrations based on in-flight data. Subsequently, in late August, updated NIRCam calibrations were calculated independently and utilized in GRIZLI v4 image processing of many public data sets, including this one. These calibrations are consistent to within <5% of the most recent `jwst_0995.pmap` calibrations in each filter and detector. We measure photometry (Section 4) in the GRIZLI v4 images, then finally apply the necessary flux corrections

[63] https://s3.amazonaws.com/grizli-v2/JwstMosaics/v4/index.html

Table 2
Photometric Recalibration

Filter	JD1, JD2	JD3
F115W	A3 0.9687	A1 0.9826
F150W	A3 0.9536	A1 0.9777
F200W	A3 0.9658	A1 0.9891
F277W	A5 1.0239	A5 1.0239
F356W	A5 0.9763	A5 0.9763
F444W	A5 1.0073	A5 1.0073

Note. We multiply JD1, 2, 3 fluxes and uncertainties by these values to correct from GRIZLI v4 calibration to `jwst_0995.pmap`.

(Table 2) to JD1 and JD2 observed in NIRCam detectors A3 and A5, and JD3 in detectors A1 and A5.[64]

The GRIZLI pipeline applies corrections for $1/f$ noise striping and masks "snowballs" caused by high-energy cosmic rays. It also corrects for stray light features known as "wisps," which are static and have been modeled in the A3, B3, and B4 detectors in F150W and F200W images.[65,66]

Finally, the GRIZLI pipeline combines all images in each filter, drizzling them to a common pixel grid using ASTRODRIZZLE (Koekemoer et al. 2003; Hoffmann et al. 2021). The NIRCam short-wavelength F115W, F150W, and F200W images are drizzled to $0\farcs02$ pixels, and all other images are drizzled to $0\farcs04$ pixels (on the same grid at half the resolution). All HST and JWST images are aligned to a common world coordinate system registered to the Gaia DR3 catalogs (Gaia Collaboration et al. 2021). We create color images using `Trilogy`[67] (Coe et al. 2012).

2.4. James Webb Space Telescope Stellar Diffraction Spikes and Scattered-light Artifacts

At relatively low Galactic latitude, $b = 25°$, there are many stars affecting the image. One particularly bright ~8th magnitude star $\sim 2'$ southwest of JD1 and JD2 (observed in module B) produces a diffraction spike that crosses the entire module A image of the cluster. Fortunately, none of the lensed images JD1, 2, 3 are impacted by the spikes, with the possible exception of one that comes close to JD2 in F277W.

Other scattered-light artifacts are isolated and do not impact the lensed images of MACS0647–JD. "Claws" are visible as horizontal stripes in our F200W image well south of JD3. These are presumably due to an extremely bright ($K \lesssim 3$ Vega mag) star very far from the field of view (10° in the telescope's V3 direction). They do not move significantly between dithers and cannot be modeled or subtracted.

Dragon's Breath Type II is visible as vertical stripes in our F200W image, near the west edge, extending south of center in the A4 detector, also far from JD1, 2, 3.[68]

3. Three Stellar Components

The JWST NIRCam images clearly resolve MACS0647–JD into two galaxies or components: A and B (Figure 3).

[64] https://zenodo.org/record/7143382
[65] https://jwst-docs.stsci.edu/data-artifacts-and-features/snowballs-artifact
[66] https://jwst-docs.stsci.edu/jwst-near-infrared-camera/nircam-features-and-caveats/nircam-claws-and-wisps
[67] https://github.com/dancoe/trilogy
[68] https://jwst-docs.stsci.edu/jwst-near-infrared-camera/nircam-features-and-caveats/nircam-claws-and-wisps

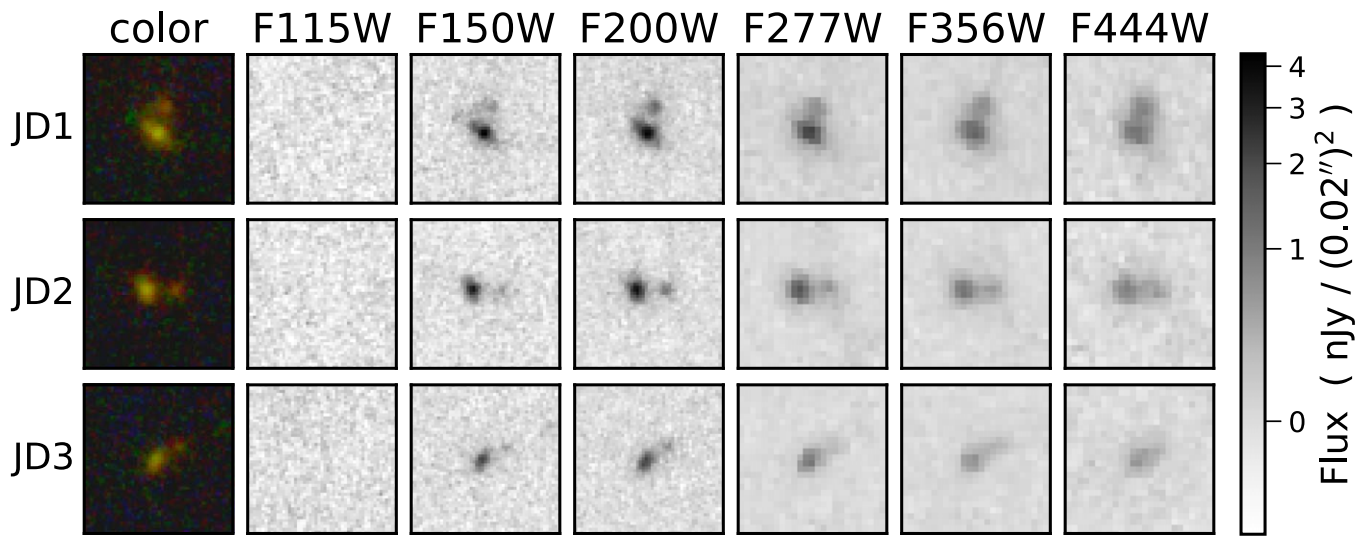

Figure 3. MACS0647–JD observed in the NIRCam SW color image (B = F115W, G = F150W, R = F200W) and in each NIRCam filter. Each image stamp is 1″ across. Grayscale images for all filters are scaled to the same flux densities per 0.″02 pixel, as shown in the color bar. Data are recalibrated to `jwst_0995.pmap`.

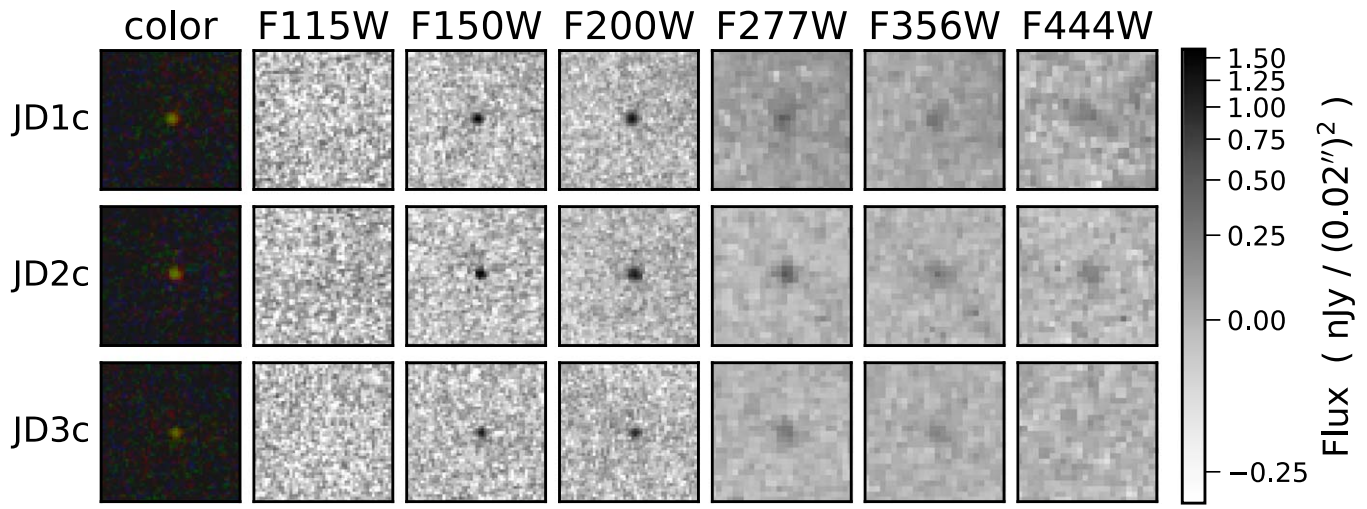

Figure 4. Candidate companion galaxy MACS0647–JDc. Color and grayscale images as in Figure 3.

Component A is brighter and spatially extended, while B is fainter, more compact, and redder in the short-wavelength filters. These two components are clearly seen in each of the three lensed images JD1, 2, 3. Both are *J*-band dropouts, not detected in F115W.[69]

Additionally, we identify a candidate companion galaxy C, another *J*-band dropout (Figure 4), observed 2.″2, 2.″2, and 0.″9 from JD1A, JD2A, and JD3A, respectively (see Figure 2). It is fainter than A and B and even more compact.

3.1. Lens Modeling

A first lens model for this cluster, prior to CLASH imaging, was presented by Zitrin et al. (2011). Lens modeling enabled by the CLASH HST images has been presented in Coe et al. (2013), Zitrin et al. (2015), and Chan et al. (2017) using various methods: Lenstool (Jullo et al. 2007; Jullo & Kneib 2009), Zitrin-LTM (Broadhurst et al. 2005; Zitrin et al. 2009), and WSLAP+ (Diego et al. 2005, 2007). Magnification estimates range from 6.0–8.4, 5.5–7.7, and 2.1–2.8 for JD1, 2, 3, respectively. Uncertainties are thus roughly ±17%, similar to performances modeling simulated lenses with excellent constraints. These models have decent constraints with between 9 and 12 multiply lensed galaxies, however none have spectroscopic redshift.

JWST imaging reveals more multiply lensed image systems, which will be published alongside a new lens model in A. K. Meena et al. (2023, in preparation). The model was obtained using a revised, analytic version of the parametric method presented in Zitrin et al. (2015) and was recently used, for example, in Pascale et al. (2022). This preliminary, new parametric lens model yields magnification estimates of ∼6.9, 6.3, and 2.1 for JD1, 2, 3, with tangential (linear) magnifications of ∼4.7, 4.4, and 1.8. Another preliminary new mass model using GLAFIC (Oguri 2010) predicts magnifications of ∼9.1, 5.5, and 1.8 for JD1, 2, 3, respectively.

JWST imaging also yields direct new measurements of the observed flux ratios ∼3.5:2.3:1 for JD1, 2, 3 based on NIRCam photometry measured in F200W and redward, averaging 340, 223, and 97 nJy (AB mag 25.1, 25.5, and 26.4). Based on these measured flux ratios, we adopt fiducial magnification estimates

[69] https://jwst-docs.stsci.edu/jwst-near-infrared-camera/nircam-features-and-caveats/nircam-dragon-s-breath-type-ii

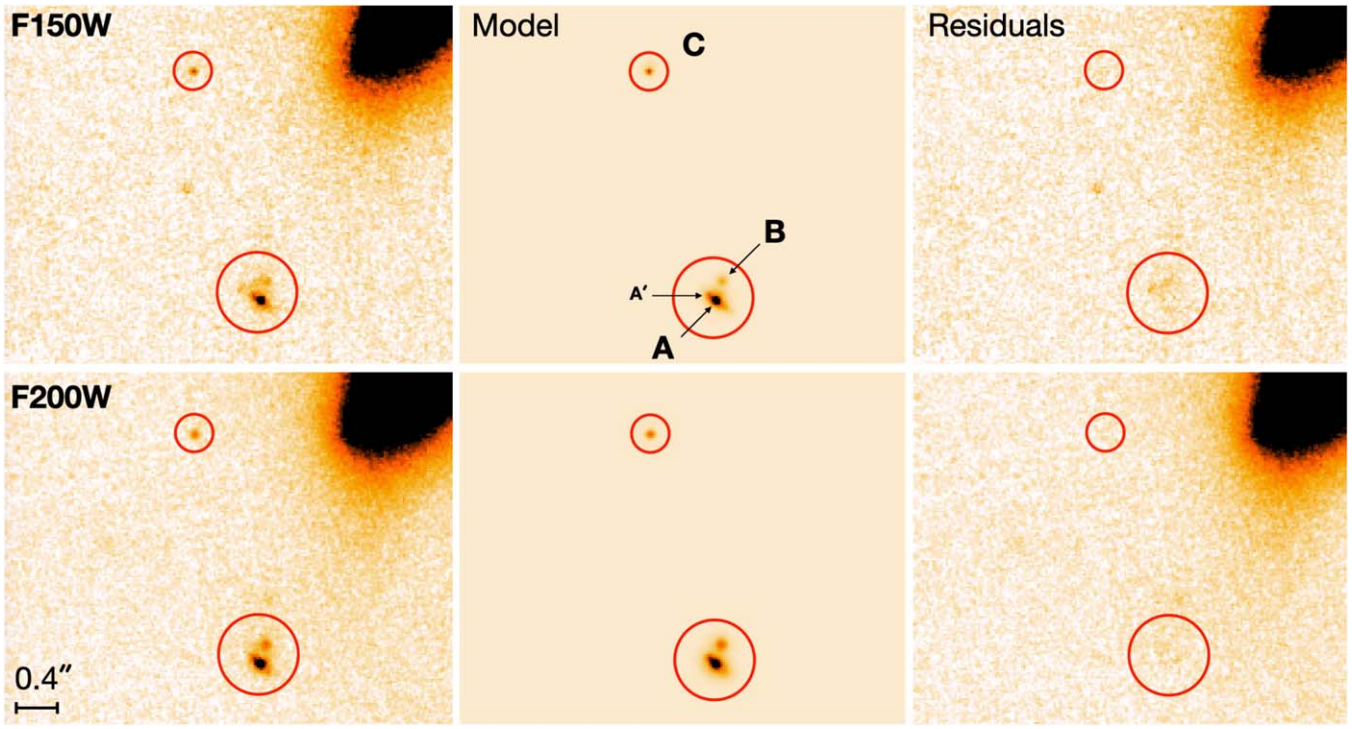

Figure 5. GALFIT modeling (center) of JD1ABC in the F150W and F200W images (left) with residuals shown at right. Sérsic model parameters are fit in F150W and held constant (aside from flux) in F200W. A possible noise fluctuation, A′, apparent only in the F150W image, was included as a fourth model component so as not to bias the fitting. A′ and C are compact and modeled as point sources (convolved with the image PSF). Based on this model combined with our lens model, we measure A and B to have radii of $\sim 70^{+24}_{-24}$ and 20^{+8}_{-5} pc, respectively (Section 3.2).

of ∼8.0, 5.3, and 2.2 for JD1, 2, 3, respectively, with tangential magnifications of ∼5, 4, and 2. These are roughly consistent with previous estimates,[70] and the total magnification ∼15.5 is roughly equal to the total in our new preliminary lens model. The average delensed flux in F200W, F277W, F356W, and F444W is 43 nJy (AB mag 27.3, $M_{\rm UV} = -20.4$) with an uncertainty of ∼17%.

3.2. Sizes and Separations

We use GALFIT (Peng et al. 2010) to model JD1 A and B in the sharpest image, F150W. Galaxy A is fit well by a two-component Sérsic model (see Figure 5), including a compact core and a more extended host with a radius of 4.4 ± 1.5 pixels $= 0\farcs09$ (adopting a Gaussian profile for both, and a Sérsic index $n = 0.5$). Delensing that by the tangential linear magnification ∼5, yields a radius $\sim 70^{+24}_{-24}$ pc. Galaxy B is fit well by a single compact source with a radius of $1.3^{+0.5}_{-0.3}$ pixels, with a delensed radius $\sim 20^{+8}_{-5}$ pc. This analysis method was tested and validated with simulations in Meštrić et al. (2022). Note that we use the morphology measurements from F150W to model the F200W image, as shown in Figure 5, and is well fitted.

A similar independent analysis with IMFIT (Erwin 2015) fitting galaxy A to a single component yields a radius of 3 pixels (with higher Sérsic index $n \sim 2$ versus 0.5 for the GALFIT extended component). This yields a smaller delensed radius ∼45 pc for A.

A third analysis measuring the curve of growth (flux versus radius) yields delensed effective radii ∼70 and 50 pc for A and B, respectively.

To measure separations between A, B, and C, we delens images JD1, 2, 3 to the source plane (Figure 6). We find the cores of A and B are separated by $\sim 0\farcs1$ ($\sim$ 400 pc) in both the Zitrin-analytic GLAFIC models. The candidate companion C is ∼3 kpc away.

4. Photometry Measurements

The GRIZLI pipeline uses SEP (Barbary 2016), a Python implementation of SourceExtractor (Bertin & Arnouts 1996), to detect sources in a stacked NIRCam image and measure aperture-matched photometry in all filters. Photometry is measured in circular apertures with radii $0\farcs5$.

JD1, 2, 3 are detected as objects #3593, 3349, and 4871 in the public v4 catalog (Section 2.3). Table 3 provides their measured coordinates and photometry recalibrated using Table 2. These are total fluxes measured for galaxies A+B. The photometry of individual galaxies A and B is organized in Table 4. To measure photometry of these components individually, we use the methods below.

The candidate companion galaxy C is detected as objects #3621, 3314, and 4858.

4.1. PIXEDFIT

To spatially resolve the SEDs of the two galaxies, we use PIXEDFIT (Abdurro'uf et al. 2021). For this resolved SED analysis, we use 13-band imaging from ACS and NIRCam (excluding ACS F850LP and WFC3/IR filters with broader point-spread functions, PSF, as well as the lower-wavelength WFC3/UVIS filters), similar to the analyses carried out in

[70] Previous magnification estimates for JD1, JD2, and JD3 were 8, 7, 3 (Coe et al. 2013); 6, 6, 2 (Zitrin et al. 2015); and 8, 8, 3 (Chan et al. 2017).

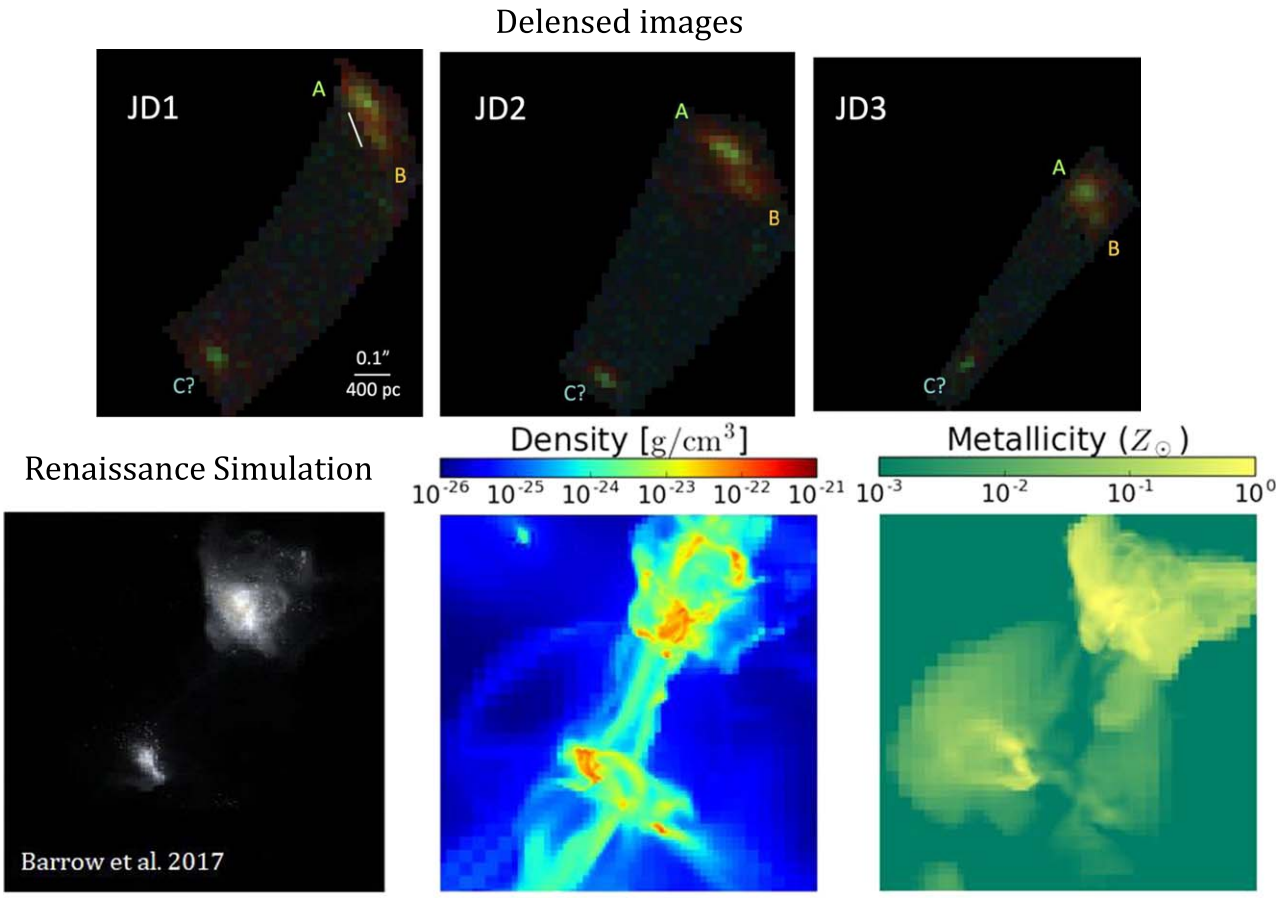

Figure 6. Delensed images of JD1, 2, 3 based on our Zitrin-analytic lens model (A. K. Meena et al. 2023, in preparation) compared to a pair of merging galaxies in the Renaissance simulations (Barrow et al. 2017), shown at bottom on the same physical scale. Galaxies A and B are separated by $\sim 0\farcs1 \sim 400$ pc in the delensed source plane. The candidate companion C is $\sim 0\farcs63 \sim 2.5$ kpc away. Note the relative positions are reproduced well here assuming A, B, and C are all at $z = 10.6$. The reconstruction is similar for C at $z \sim 9$, with delensed positions changing slightly. Redshifts $z < 5$ are ruled out for B and C (assuming A is at $z \sim 11$), as the relative separations would change significantly.

Abdurro'uf et al. (2023). First, all images are resampled to $0\farcs02$ pixels using `reproject` (Robitaille et al. 2020). Then, we use SEP (Barbary 2016) to detect objects in the NIRCam images, generating a segmentation map defining pixels belonging to A+B.

Photometry is measured in elliptical apertures defined within the segments and without overlap. Aperture A is an ellipse with semimajor axis $0\farcs2$ and semiminor axis $0\farcs1$. Aperture B is a circle with radius $0\farcs1$. Radial profiles decrease within these apertures, reaching a minimum between them that defines their boundary.

We initially forgo PSF matching to retain spatial resolution. However, we note measured colors may be affected by lost and/or blended flux in the redder filters. The F444W PSF FWHM is $0\farcs14$ with 54% encircled energy within $r = 0\farcs1$, compared to 70% for F150W.[71] We perform aperture corrections based on point-source encircled energy and discuss how this affects the results below. The effect is to make colors redder, though we note this may be an overcorrection with flux also blending between A and B.

Aside from A and B, there are no other nearby objects affecting the photometry. Local backgrounds are small, consistent with zero, and not subtracted.

[71] https://jwst-docs.stsci.edu/jwst-near-infrared-camera/nircam-performance/nircam-point-spread-functions

4.2. IMFIT

IMFIT (Erwin 2015) has been used to perform 2D fitting to MACS0647–JD. The PSF used in the fitting has been generated, for each filter, using isolated stars. The two clumps have been fitted separately, alternately masking them, followed by a simultaneous fitting step with the parameters for clump A kept fixed. A Sérsic profile has been used for clump A, while for clump B both Sérsic and point-like profiles resulted in similar values for the reduced χ^2. Photometry has then been performed on the models generated from the results from the 2D fitting, using an elliptical aperture for clump A.

4.3. Chebyshev–Fourier Functions

CHEFs (from Chebyshev–Fourier functions; Jiménez-Teja & Benítez 2012) are a mathematical orthonormal basis specially designed to model the surface luminous distribution of galaxies. First, a segmentation map is created using SourceExtractor (Bertin & Arnouts 1996) to identify the regions that are dominated by each object. Then, objects are sorted by magnitude and fitted with CHEFs, so the light contribution from the brightest objects is removed previous to the modeling of the fainter objects. As CHEFs are an orthonormal basis, they can fit any shape, thus recovering all the light even in the case of irregular morphologies. The CHEFs model of each object is calculated in a circular region

Table 3
Coordinates and Multiwavelength Photometry of MACS0647–JD

Filter	JD1	JD2	JD3
R.A.(J2000)	101.9822676	101.971326	101.9811153
Decl.(J2000)	70.24328239	70.2397157	70.26059029
F275W	-31 ± 35	11 ± 30	43 ± 27
F336W	-8 ± 27	32 ± 24	-24 ± 21
F390W	-12 ± 17	-5 ± 44	24 ± 23
F435W	-25 ± 21	70 ± 18	-23 ± 21
F475W	7 ± 15	-26 ± 113	21 ± 12
F555W	-2 ± 10	15 ± 8	8 ± 7
F606W	-16 ± 10	4 ± 12	-1 ± 28
F625W	-38 ± 20	-24 ± 17	15 ± 17
F775W	24 ± 28	-16 ± 21	-18 ± 17
F814W	-8 ± 9	0 ± 8	-3 ± 7
F850LP	-55 ± 33	-11 ± 30	29 ± 30
F105W	3 ± 19	4 ± 16	-1 ± 14
F110W	-25 ± 13	5 ± 12	7 ± 10
F115W	-1 ± 8	-35 ± 7	-2 ± 6
F125W	-13 ± 19	-9 ± 17	6 ± 14
F140W	126 ± 11	97 ± 12	59 ± 9
F150W	304 ± 7	173 ± 6	92 ± 5
F160W	301 ± 17	203 ± 17	85 ± 13
F200W	354 ± 6	227 ± 6	115 ± 4
F277W	351 ± 6	248 ± 5	93 ± 3
F356W	322 ± 6	203 ± 5	86 ± 3
F444W	330 ± 9	214 ± 7	95 ± 5

Note. All fluxes are given in nanojansky.

Table 4
Multiwavelength Photometry of Two Individual Galaxies in MACS0647–JD (i.e., JDa and JDb)

Filter	JD1a	JD1b	JD2a	JD2b	JD3a	JD3b
F435W	-16 ± 6	-2 ± 5	4 ± 5	8 ± 5	-5 ± 4	-3 ± 4
F475W	-9 ± 5	-2 ± 3	-10 ± 4	-9 ± 3	-3 ± 3	0 ± 2
F555W	-10 ± 3	-5 ± 2	-3 ± 3	-5 ± 2	-1 ± 2	-2 ± 1
F606W	-6 ± 7	-2 ± 4	0 ± 4	-1 ± 3	6 ± 14	1 ± 3
F625W	-19 ± 7	-4 ± 4	2 ± 5	-6 ± 4	8 ± 5	-3 ± 2
F775W	-23 ± 9	-6 ± 8	-25 ± 6	3 ± 5	-8 ± 5	-3 ± 3
F814W	-15 ± 4	-5 ± 3	-8 ± 3	-4 ± 2	-1 ± 2	-1 ± 2
F115W	-18 ± 3	-2 ± 2	-10 ± 3	-7 ± 2	-2 ± 2	-3 ± 1
F150W	144 ± 3	27 ± 2	91 ± 3	16 ± 2	55 ± 2	7 ± 1
F200W	160 ± 3	43 ± 2	115 ± 2	27 ± 2	60 ± 2	13 ± 1
F277W	143 ± 2	37 ± 2	90 ± 2	27 ± 1	43 ± 1	8 ± 1
F356W	106 ± 2	39 ± 1	64 ± 2	25 ± 1	30 ± 1	9 ± 1
F444W	97 ± 3	44 ± 2	59 ± 2	26 ± 1	28 ± 1	8 ± 1

Note. All fluxes are described in nanojansky and were measured using PIXEDFIT (Abdurro'uf et al. 2021).

with radius twice the equivalent radius of the area assigned to the object by the segmentation map. However, the flux is measured up to the radius where the profile of the model either converges to zero or submerges into the sky noise.

5. Spectral Energy Distribution Fitting

We perform SED fitting with various methods to estimate the photometric redshift and physical parameters of MACS0647–JD. The various methods adopt different SED templates and assumptions about the physical parameters, summarized in Table 5. We also match the observed clump colors to simulated galaxies with realistic bursty SFHs (Section 5.6).

5.1. EAZY

Our public data set includes SED-fitting results from EAZY (Brammer et al. 2008) using recently implemented SFHZ templates with redshift-dependent SFHs.[72] EAZY fits non-negative linear combinations of these templates to the observed photometry. The code is fast, analyzing thousands of galaxies in minutes. It estimates photometric redshifts $z = 10.6^{+0.3}_{-0.2}$, $z = 10.6^{+0.3}_{-0.4}$, and $z = 10.2^{+0.5}_{-0.6}$ (95% C.L.) for JD1, 2, 3, respectively (A+B components combined, with F200W AB mag 25.0, 25.5, and 26.2).

The fainter companion galaxy C (F200W AB mag 28.0, 27.3, and 27.8 with large uncertainties) is also a *J*-band dropout that can be well fit to SEDs at $z = 10.6$ given its larger photometric uncertainties, as we show in Section 6.6. The photometric redshifts are highly uncertain, with 95% confidence ranges 0.5–10.2, 2.2–10.3, and 9.8–11.5 for JD1C, JD2C, and JD3C, respectively.

While EAZY also provides quick estimates of physical parameters, we turn to other methods to more fully explore the parameter space and estimate values with uncertainties for the individual clumps A and B.

5.2. Bagpipes

Bagpipes[73] (Carnall et al. 2018) fits redshift along with a multidimensional space of physical parameters using the MultiNest nested sampling algorithm (Feroz & Hobson 2008; Feroz et al. 2009; Feroz & Skilling 2013). We run Bagpipes with various sets of assumptions.

We use BPASS v2.2.1 SED templates (Eldridge & Stanway 2009), importantly including binary stars, resulting in brighter rest-UV flux (Eldridge 2020; Eldridge & Stanway 2022). We use the fiducial BPASS initial mass function (IMF) imf135_300 (Kroupa et al. 1993) slope $\alpha = -2.35$ between 0.5 and 300 $M_\odot$ and a shallower $\alpha = -1.3$ for lower-mass stars 0.1–0.5 $M_\odot$. This is close to the shallower upper-mass slope IMF of Kroupa (2002). Metallicities range from (0.0005–2) $Z_\odot$.

We reprocess the templates using the photoionization code CLOUDY c17.03 (Ferland et al. 1998, 2013, 2017) to include nebular continuum and emission lines. We generate templates for the ionization parameter U ranging between $\log(U) = -4$ to -1.

We assume an analytic SFH model, "delayed τ": SFR $(t) \propto t \exp(-t/\tau)$. The star formation rate (SFR) rises linearly, then slows before declining exponentially, unless the free parameter τ is larger than the formation age (as in our fits), in which case there is no decline.

For dust attenuation, we use the Salim et al. (2018) parameterization with slope δ allowed to vary between 0 (Milky Way) and steeper -0.45 (Small Magellanic Cloud, SMC), and 2175 Å bump strength B allowed to vary between 0 and 5 (where the Milky Way has $B = 3$ and the SMC has $B \sim 0$). Young stars (age <10 Myr) residing in stellar birth clouds experience more dust extinction by a factor η in the range 1–3.

[72] https://github.com/gbrammer/eazy-photoz/tree/master/templates/sfhz
[73] https://bagpipes.readthedocs.io

Table 5
SED-fitting Methods, Templates, and Assumptions Used

Method	SEDs	IMF	SFH	Dust	Ionization $\log(U)$
EAZY	SFHZ				
Bagpipes	BPASS+CLOUDY	Kroupa et al. (1993)	Delayed τ	Salim et al. (2018)	-4 to -1
PIXEDFIT	FSPS+CLOUDY	Chabrier (2003)	Double power law	Charlot & Fall (2000)	-2
Prospector	FSPS+CLOUDY	Chabrier (2003)	Constant/nonparametric	SMC (Pei 1992)	-4 to -1
BEAGLE	BC03+CLOUDY	Chabrier (2003)	Constant	SMC (Pei 1992)	-4 to -1

5.3. PIXEDFIT

As an independent comparison, we also perform SED fitting using PIXEDFIT (Abdurro'uf et al. 2021). For SED modeling, we use Flexible Stellar Population Synthesis (FSPS;[74] Conroy et al. 2009; Leja et al. 2017), the IMF of Chabrier (2003), Padova isochrones (Girardi et al. 2000; Marigo & Girardi 2007; Marigo et al. 2008), the MILES stellar spectral library (Sanchez-Blazquez et al. 2006; Falcón-Barroso et al. 2011), and the two-component dust attenuation law by Charlot & Fall (2000). We assume a parametric SFH model in the form of a double power law. FSPS incorporates CLOUDY code for modeling the nebular emission. We model the attenuation due to the intergalactic medium (IGM) using Inoue et al.'s (2014) model. We assume uniform priors for redshift (2.0–15.0), age (0.01–10.0 Gyr), Z ($\log(Z/Z_\odot)$: $[-2.0, 0.2]$), and SFH timescale τ (0.1–32 Gyr). The fitting with the double power-law SFH has two more free parameters that control the slopes of the rising and falling star formation episodes (β and α). We assume a uniform prior for these parameters with a range of $10^{-2.0}$–$10^{2.0}$. For the fitting method, we apply a Markov Chain Monte Carlo method and set the number of walkers and steps to be 100 and 1000, respectively.

5.4. Prospector

To get an independent comparison with nonparametric SFH models, we run SED fitting using Prospector (Leja et al. 2017; Johnson et al. 2021), adopting both constant and nonparametric SFHs. Similar to PIXEDFIT, this code uses FSPS stellar population synthesis models and CLOUDY code to account for the nebular emission. We assume a Chabrier (2003) IMF with mass range 0.1–300 $M_\odot$, and the IGM attenuation model of Inoue et al. (2014). We assume a uniform prior for redshift ($z = 6$–15), and log-uniform priors for stellar mass ($5 \leqslant \log(M/M_\odot) \leqslant 12$), V-band optical depth assuming a SMC dust extinction law ($-3 \leqslant \log(\tau_V) \leqslant 0.7$; Pei 1992), stellar metallicity ($-2.2 \leqslant \log(Z/Z_\odot) \leqslant -0.3$; we further assume that the interstellar gas-phase metallicity is equal to the stellar metallicity), and ionization parameter $-4 \leqslant \log(U) \leqslant -1$. For our constant SFH model, we assume a log-uniform prior on formation age from 1 Myr to the age of the universe at the redshift under consideration. Throughout this process, we remove Lyα from the fitting templates.

The nonparametric SFH models implemented in Prospector are piecewise constant functions in time. We adopt eight time bins spanning from the time of observation to a formation redshift, $z_{\rm form} = 15$–30 (uniform prior), where the two most recent bins range from 0–3 to 3–10 Myr and the remaining six are spaced evenly in logarithmic lookback time. We adopt the "continuity" prior in Prospector, which tends to weight against sharp changes in SFR between adjacent time bins, though we note that the choice of nonparametric prior can have a significant influence on the inferred physical parameters (e.g., Leja et al. 2019; Tacchella et al. 2022; Whitler et al. 2023b).

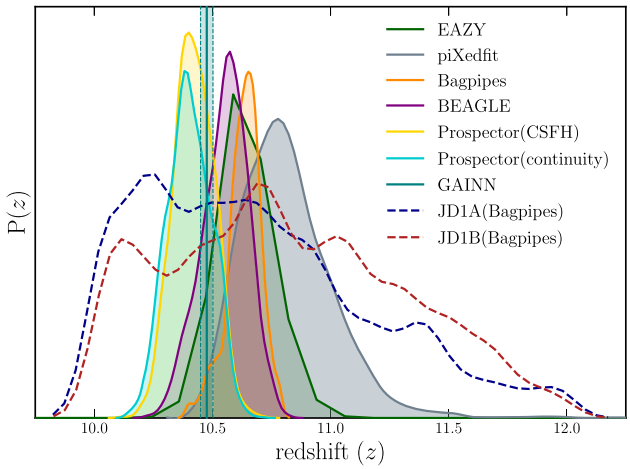

Figure 7. Redshift likelihood distributions $P(z)$ of JD1 A+B estimated by various methods (Section 6.1). Also shown are Bagpipes results for the individual clumps A and B.

5.5. BEAGLE

We also perform SED fitting using the BEAGLE tool (Chevallard & Charlot 2016). BEAGLE uses templates by Gutkin et al. (2016), which combines the 2016 version of BC03 with the CLOUDY code to incorporate nebular emission. We assume a constant SFH model and fit for age with a uniform prior ranging from 1 Myr to the age of the universe at the redshift under consideration. We adopt the same priors on redshift, stellar mass, τ_V, Z, and $\log(U)$ as for the nonparametric Prospector models. We assume that the total interstellar (dust- and gas-phase) metallicity is equal to the stellar metallicity, but note that BEAGLE self-consistently accounts for the depletion of metals onto dust grains, regulated in part by the dust-to-metal mass ratio (ξ_d), which we fix to $\xi_d = 0.3$.

5.6. GAINN

Finally, we identified simulated galaxies with colors similar to those observed for MACS0647–JD to estimate its redshift and SFH. We analyzed detailed ENZO (Bryan et al. 2014) star-forming radiative-hydrodynamic simulations of the early universe with synthetic photometry generated by Barrow et al. (2020). The simulated galaxy redshifts and colors were used as a training set for the Galaxy Assembly and Interaction Neural Network (GAINN; Santos-Olmsted et al. 2023). Additional details are provided in Appendix A.3 and results are presented below.

[74] https://github.com/cconroy20/fsps

Table 6
Physical Properties of MACS0647–JD Estimated from Bagpipes Corrected for Magnification (Flux Ratio)

	JD1	JD2	JD3	Combined
Formation age (Myr)	160^{+69}_{-69}	151^{+60}_{-74}	153^{+121}_{-75}	177^{+73}_{-71}
Mass-weighted age (Myr)	54^{+24}_{-23}	51^{+20}_{-25}	51^{+43}_{-25}	59^{+25}_{-24}
Stellar mass ($\log(M_*/M_\odot)$)	$8.62^{+0.11}_{-0.15}$	$8.61^{+0.10}_{-0.18}$	$8.51^{+0.18}_{-0.22}$	$8.65^{+0.11}_{-0.14}$
SFR ($M_\odot$ yr^{-1}) within 100 Myr	4^{+1}_{-1}	4^{+1}_{-1}	3^{+1}_{-1}	4^{+1}_{-1}
log sSFR (yr^{-1})	$-7.98^{+0.05}_{-0.09}$	$-7.96^{+0.04}_{-0.08}$	$-7.97^{+0.04}_{-0.16}$	$-8.00^{+0.07}_{-0.10}$
Photometric redshift	$10.64^{+0.06}_{-0.07}$	$10.76^{+0.08}_{-0.09}$	$10.50^{+0.14}_{-0.16}$	$10.65^{+0.09}_{-0.10}$
Relative flux (⩾F200W)	1	0.66	0.28	1.94
Magnification (flux ratio)	8	5.3	2.2	15.5
Magnification (lens model)	6.9	6.3	2.1	15.3
Tangential magnification	4.7	4.4	1.8	

Note. Magnification uncertainties are on the order of 15% (Meneghetti et al. 2017) and are not included in the uncertainties quoted above for stellar mass and SFR.

6. Results and Discussion

6.1. Photometric Redshift

MACS0647–JD is confidently at $z = 10.6 \pm 0.3$ (Figure 7), with this range spanning the most likely redshifts from five SED-fitting packages as well as the GAINN deep-learning network, which estimates $z = 10.48$, 10.81, and 10.54 for JD1, 2, 3, respectively. The components A and B are also each independently strong $z \sim 11$ candidates (with no significant likelihood below $z < 9.5$), despite lower signal-to-noise ratio photometry in each individual object.

We also tried restricting $z < 9$ with Bagpipes, finding significantly worse ($\chi^2 \sim 500$) fits at $z \sim 0.2$ for JD1, 2, 3 (that reproduce the flat NIRCam colors at 2–5 μm but miss the NIRCam F150W and F115W photometry, also failing to drop out in bluer filters). Dusty/old galaxies at $z \sim 2$–5 have SEDs that are far too red, with SEDs rising through the near-IR.

6.2. Physical Properties

In Table 6, we report the physical properties of MACS0647–JD treated as a single galaxy analyzed by Bagpipes with photometry from the GRIZLI v4 catalog (recalibrated). SED fits are shown in Figure 8. We report results for each of the three lensed images JD1, 2, 3 and for the stacked photometry, correcting SFR and mass for magnification. Assuming A+B had the same SFH, this analysis estimates a mass-weighted age 60 ± 25 Myr, with a SFR 4 ± 1 $M_\odot$ yr^{-1} averaged over 100 Myr, a stellar mass between 3–6 $\times 10^8$ $M_\odot$, and a sSFR $\sim$10 Gyr^{-1} ($\pm$10%). We acknowledge the stellar masses estimates are subject to uncertainties in the SFH, stellar mass function, stellar metallicities, and dust properties.

The SFR and stellar mass are consistent with the predicted stellar main sequence from semi-analytic models (Dayal et al. 2014, 2022; Yung et al. 2019) and simulations (Dekel et al. 2013; Whitaker et al. 2014; Tacchella et al. 2018; Behroozi et al. 2019). We plot these relations and results from other $z \sim 9$–12 candidates measured in JWST observations in Figure 9.

The sSFR is also consistent with predictions at this redshift, as shown in Figure 10. Note in these model predictions (Dekel et al. 2013; Whitaker et al. 2014; Tacchella et al. 2018; Behroozi et al. 2019; Dayal et al. 2022) that the sSFR is relatively flat at high redshifts, increasing only 0.2 dex from $z = 6$ to 11. This suggests a significant role for mergers in the early universe; sSFR(z) would continue to rise more as $\propto (1+z)^{2.25}$ if growth were dominated by cold-mode accretion (e.g., Dekel et al. 2009).

6.3. Components A and B: Ages, Dust, and Mass

In Table 7, we report results for components A and B analyzed individually by various SED-fitting methods with photometry from PIXEDFIT. The fiducial values are organized in Table 8. SED fits from Bagpipes are plotted in Figure 11. The corner plots of A and B are provided in Figure 12. SFHs from SED-fitting methods are plotted in Figure 13. SFHs from simulated galaxies matching the colors of A and B using GAINN are plotted in Figure 14.

B's redder color may be explained by age and/or dust. Results vary depending on the method and assumptions, including SFH. Dust is negligible ($A_V < 0.02$ mag) for A in most analyses, and slightly higher ($A_V \sim 0.1$ mag) for B, assuming steep SMC-like attenuation strongly suppressing the rest-UV.

Stellar mass estimates are on the order of 10^8 $M_\odot$ with some agreement on higher mass for clump A by a factor of 2 or more (e.g., A $\sim 2 \times 10^8$ $M_\odot$; B $\sim 10^8$ $M_\odot$).

Mass-weighted ages from the SED-fitting methods range up to $\sim$50 Myr and $\sim$100 Myr for A and B, respectively. GAINN analog simulated galaxies, similarly, have mass-weighted ages 50 ± 5 Myr and 125^{+24}_{-12} Myr for A and B, respectively.

B's SED was relatively rare among the simulated galaxies. It was best matched by galaxies that formed most of their stars over 80 Myr prior to observation, then either remained less active (<0.01 $M_\odot$ yr^{-1}) or perhaps had some shorter burst of star formation. The simulated galaxies with colors similar to A had dissimilar star formation, being bursty during that period when B was less active.

JD1A is intrinsically very blue ($\beta \sim -2.6 \pm 0.1$) as measured with a power-law fit to the F200W, F277W, and F356W photometry measured by PIXEDFIT, where β is the rest-frame UV continuum slope $F_\lambda \propto \lambda^\beta$ (or $F_\nu \propto \lambda^{\beta+2}$). We measure $\beta = -2.69$ without PSF correction and $\beta = -2.54$ after correcting for point-source encircled energy within $r = 0\farcs2$ (see Section 4.1).

Other recent JWST observations have revealed even bluer slopes ($\beta \sim -3$) in galaxies at $z \sim 7$–8.5 (Topping et al. 2022) and in a candidate $z \sim 16$ galaxy (Furtak et al. 2023), all with stellar masses on the order of 10^8 $M_\odot$. Topping et al. (2022) found these blue colors required large escape fractions, $f_{\rm esc,H\,II} \sim 0.6$–0.8, of photons leaking directly from stellar H II regions, bypassing nebular reprocessing. Our measured $\beta \sim -2.6 \pm 0.1$ is slightly redder and can be fit by our SED models that all assume $f_{\rm esc} = 0$. Nevertheless, it is in the regime where some significant $f_{\rm esc}$ should be considered to avoid biasing age and mass measurements.

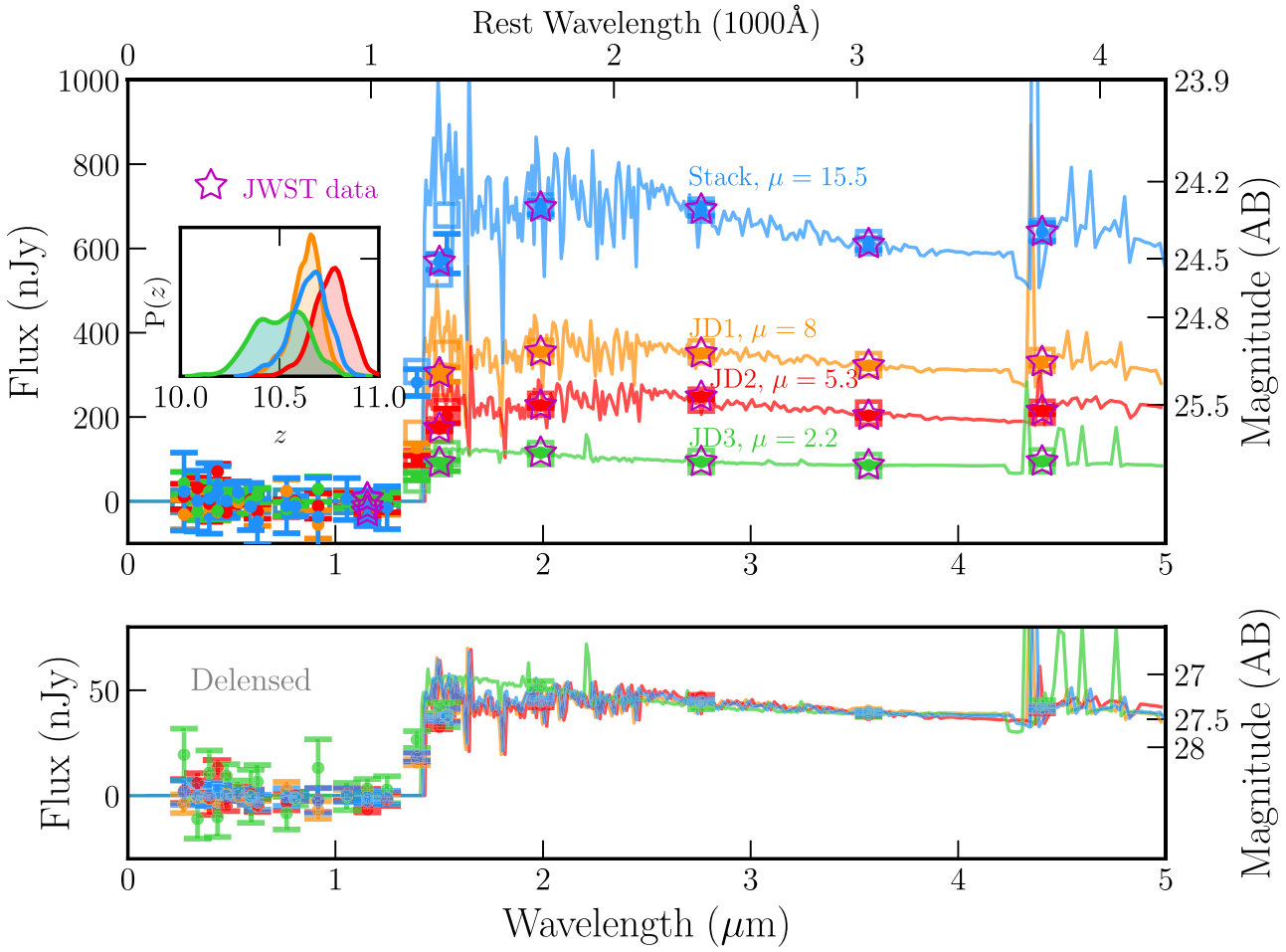

Figure 8. Photometry and `Bagpipes` BPASS SED fits for JD1, 2, 3, both as observed and delensed by fiducial magnifications $\mu = 8.0$, 5.3, and 2.2. Filled circles with error bars give measured photometry in each filter, and open boxes show model fluxes for each best-fit SED model spectrum shown. JWST photometry is highlighted by magenta stars. The $P(z)$ of JD1, 2, 3, as well as the stacked one, is shown in the small box in the upper panel.

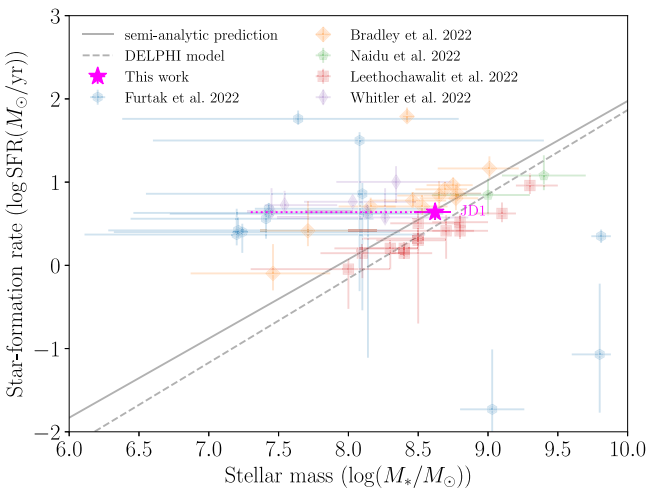

Figure 9. Star formation rate (SFR) vs. stellar mass for MACS0647–JD and recently discovered $z \sim 9$–12 candidates analyzed in JWST imaging (Bradley et al. 2022; Furtak et al. 2023; Leethochawalit et al. 2023; Naidu et al. 2022). We plot `Bagpipes` results for JD1 (A+B). The results lie along predictions for the $z = 10$ star formation main sequence from semi-analytic modeling (Yung et al. 2019) and DELPHI simulations (Dayal et al. 2014, 2022). Note that we show the stellar mass estimated from delayed τ SFH for JD1 (A+B). Possible systematic uncertainty from different assumed SFH is shown in a dotted line.

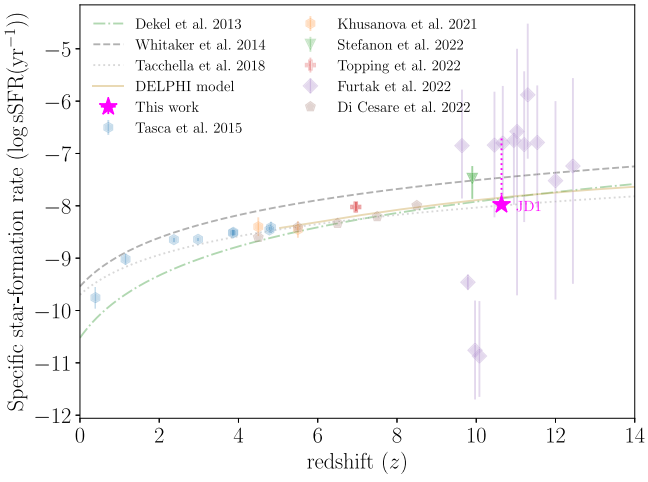

Figure 10. Specific SFR (sSFR) as a function of redshift. We show the `Bagpipes` result for the JD1 photometry, while acknowledging the results vary from different methods. We compare with published results from Tasca et al. (2015; $\log(M_*/M_\odot) > 9.7$), Khusanova et al. (2021; $9.6 < \log(M_*/M_\odot) < 9.8$), Stefanon et al. (2023; $\log(M_*/M_\odot) \sim 8.4$), Topping et al. (2022), Furtak et al. (2023), and and Di Cesare et al. (2023). We also compare with predictions from Dekel et al. (2013), Whitaker et al. (2014), Tacchella et al. (2018), and DELPHI (Dayal et al. 2014, 2022). Note that we show the stellar mass estimated from delayed τ SFH for JD1 (A+B). Possible systematic uncertainty from different assumed SFH is shown in a dotted line.

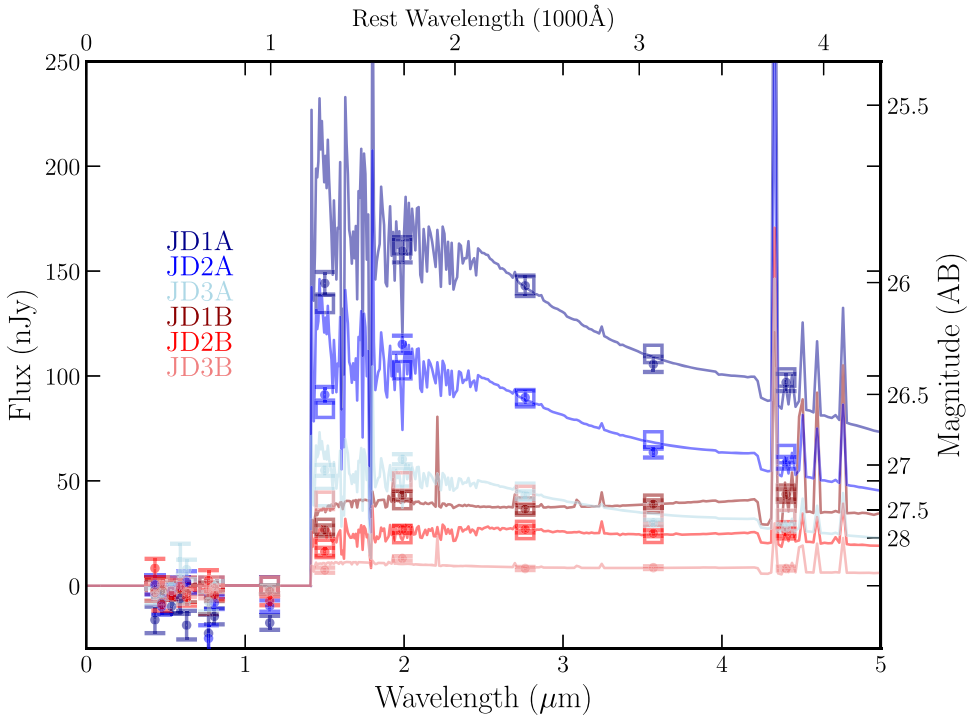

Figure 11. `Bagpipes` SED fits to photometry of individual clumps A and B measured by PIXEDFIT with 3% uncertainty added in quadrature.

Table 7
Physical Properties of A and B Analyzed Individually by Various Methods Assuming $z = 10.6$

Clump	Photometric Uncertainty	Method	SFH	Age[a] Myr	Stellar Mass $\log(M_*/M_\odot)$	Specific SFR[b] (Gyr^{-1})	Dust A_V mag	χ^2
JD1A	⋯	Bagpipes	Delayed τ exponential	1.3 ± 0.2	7.2 ± 0.1	101^{+1}_{-1}	$0.00^{+0.01}_{-0.00}$	93
	+3%	Bagpipes	Delayed τ exponential	1^{+1}_{-1}	$7.2^{+0.1}_{-0.1}$	101^{+1}_{-1}	$0.00^{+0.01}_{-0.00}$	82
	+10%	Bagpipes	Delayed τ exponential	14^{+14}_{-9}	$7.7^{+0.2}_{-0.3}$	48^{+52}_{-22}	$0.01^{+0.02}_{-0.01}$	67
	⋯	PIXEDFIT	Double power law	23^{+19}_{-9}	$8.2^{+0.1}_{-0.1}$	8^{+9}_{-7}	$0.34^{+0.22}_{-0.21}$	105
	⋯	Prospector	Nonparametric cont.	43^{+25}_{-20}	8.3 ± 0.1	0	$0.01^{+0.02}_{-0.01}$	18[c]
	⋯	Prospector	Constant	35^{+8}_{-6}	8.0 ± 0.1	14 ± 3	$0.00^{+0.00}_{-0.00}$	90[c]
	⋯	BEAGLE	Constant	35 ± 7	8.1 ± 0.1	14^{+4}_{-3}	$0.00^{+0.00}_{-0.00}$	103[c]
JD1B	⋯	Bagpipes	Delayed τ exponential	70^{+49}_{-44}	$7.8^{+0.1}_{-0.3}$	11^{+16}_{-4}	$0.10^{+0.06}_{-0.03}$	15
	+3%	Bagpipes	Delayed τ exponential	67^{+45}_{-40}	$7.8^{+0.2}_{-0.3}$	12^{+16}_{-5}	$0.10^{+0.07}_{-0.04}$	14
	+10%	Bagpipes	Delayed τ exponential	81^{+41}_{-50}	$7.8^{+0.1}_{-0.3}$	10^{+14}_{-3}	$0.10^{+0.08}_{-0.05}$	12
	⋯	PIXEDFIT	Double power law	111^{+32}_{-30}	$8.3^{+0.1}_{-0.3}$	0^{+2}_{-0}	$0.25^{+0.14}_{-0.15}$	20
	⋯	Prospector	Nonparametric cont.	127^{+50}_{-58}	8.1 ± 0.2	3^{+10}_{-2}	$0.12^{+0.12}_{-0.08}$	2.9[c]
	⋯	Prospector	Constant	3^{+35}_{-2}	6.9 ± 0.2	185^{+319}_{-171}	$0.03^{+0.03}_{-0.02}$	1.5[c]
	⋯	BEAGLE	Constant	10^{+49}_{-8}	7.3 ± 0.6	51^{+198}_{-42}	$0.01^{+0.03}_{-0.01}$	0.6[c]

Notes. Photometry is measured in the brightest image JD1 by PIXEDFIT, analyzed with and without inflated uncertainties and corrected for magnification. Most of these SED-fitting methods assume a Chabrier (2003) IMF (Table 5). BAGPIPES assumes a Kroupa et al. (1993) IMF; to renormalize those results, we multiplied the stellar masses by 0.94 (Madau & Dickinson 2014).
[a] Mass weighted.
[b] Within recent 10 Myr.
[c] Calculated in F200W and redder photometry.

Table 8
Estimated Clump Properties Adopting Fiducial Stellar Mass and SFR

Clump	Radius	Stellar Mass	Stellar Mass Density	SFR	SFR Density
JD1A	70^{+24}_{-24} pc	$10^8\ M_\odot$	1800 $M_\odot$ pc^{-2}	1 $M_\odot$ yr^{-1}	18 $M_\odot$ yr^{-1} kpc^{-2}
JD1B	20^{+8}_{-5} pc	$6 \times 10^7\ M_\odot$	12,000 $M_\odot$ pc^{-2}	0.6 $M_\odot$ yr^{-1}	120 $M_\odot$ yr^{-1} kpc^{-2}

Note. The estimated stellar mass and SFR vary from different SED-fitting packages under different assumptions (e.g., SFH). The uncertainties of stellar mass density and SFR density may be up to 200%.

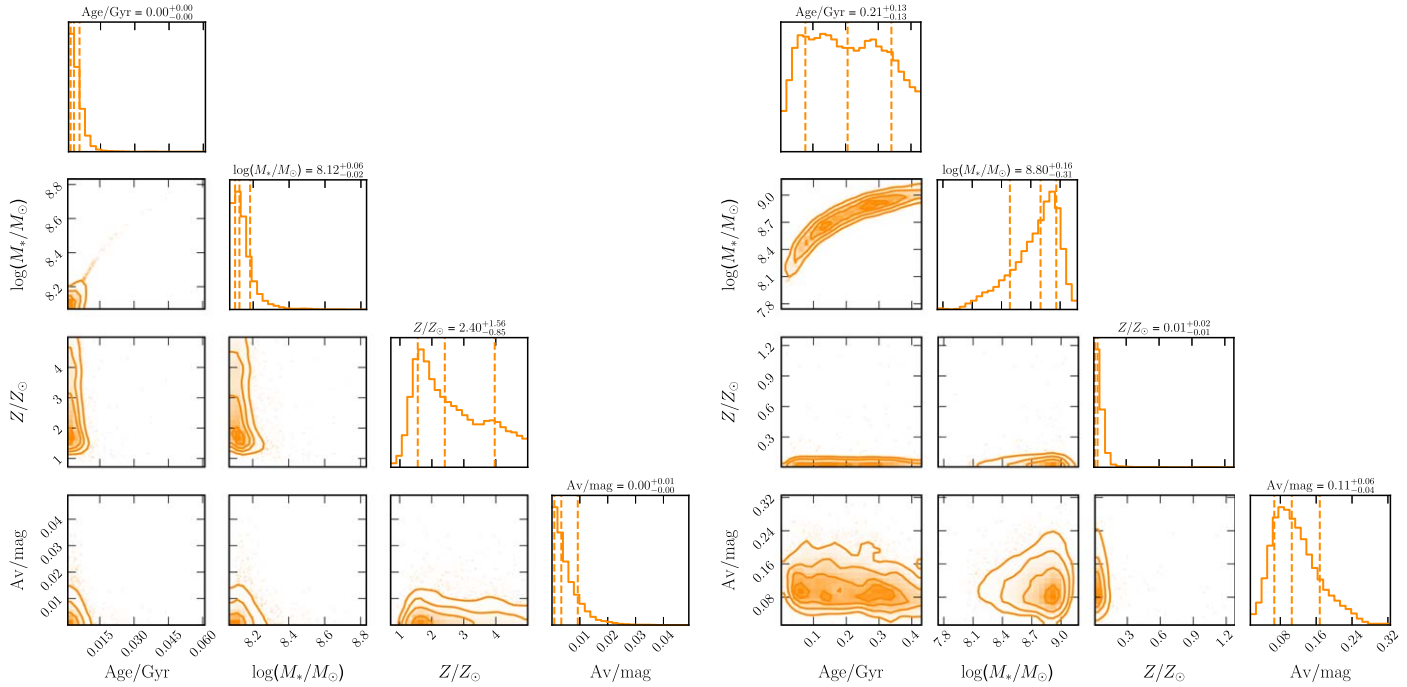

Figure 12. Constraints on age, stellar mass, metallicity, and dust for JD1A (left) and JD1B (right) from `Bagpipes` with +3% uncertainty. Note that the mass estimates shown here are not delensed.

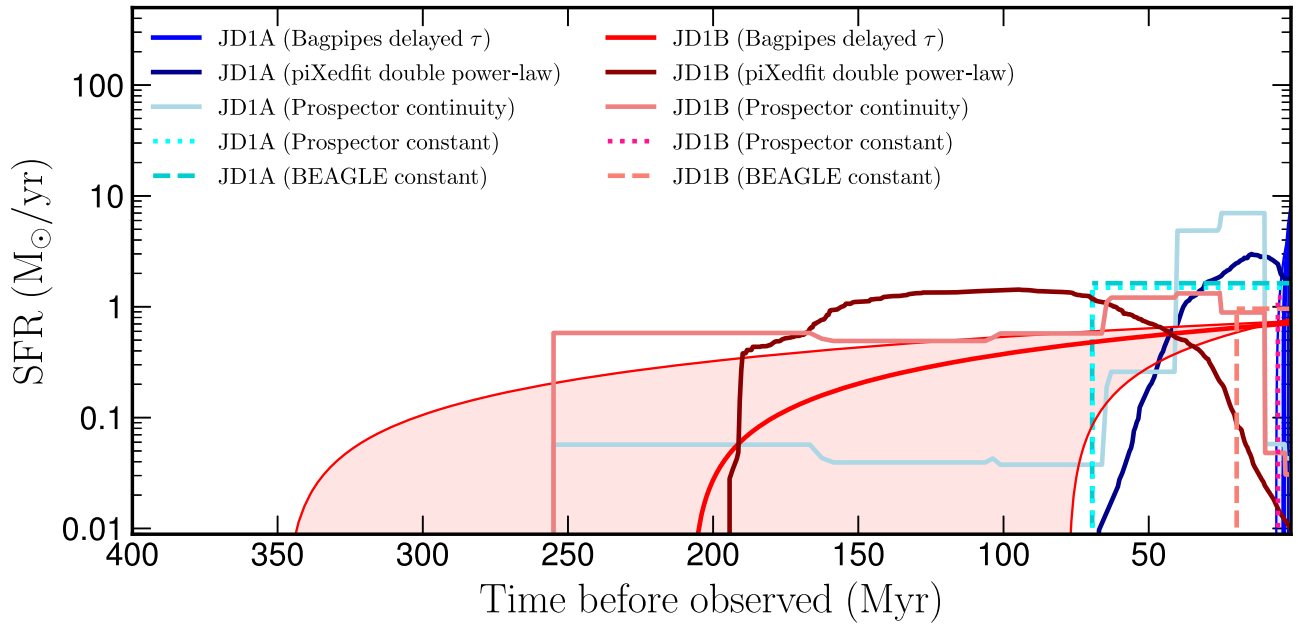

Figure 13. Star formation histories (SFHs) of clumps A and B for the median ages estimated by each method. The various SFH parameterizations and assumptions are summarized in Table 7. For `Bagpipes`, we plot results from adding 3% photometric uncertainty. Shaded regions indicate the 68th percentile confidence intervals.

Binary stars are important to include in SED modeling as in BPASS, especially for such blue galaxies (Eldridge 2020; Eldridge & Stanway 2022). Binary interactions produce more Wolf–Rayet/helium stars at later ages, generating more energetic photons. Thus, blue observed SEDs may be fit well by older (tens of millions of years) BPASS templates including binaries, whereas templates without binaries may require very young ages (<10 Myr).

We also note uncertainty in the photometry and some variation in β measured by the various methods and in the three lensed images. Ultimately, upcoming NIRSpec spectroscopy will improve measures of β and age, and reveal other signatures of large escape fractions.

6.4. Stellar Mass and Star Formation Rate Densities

The stellar complexes in MACS0647–JD are very dense, with $\sim 10^8\,M_\odot$ stellar mass packed into effective radii of $\sim 70^{+24}_{-24}$ and 20^{+8}_{-5} pc for A and B, respectively. Assuming fiducial masses 10^8 and $6\times10^7\,M_\odot$ for A and B, respectively, the stellar mass

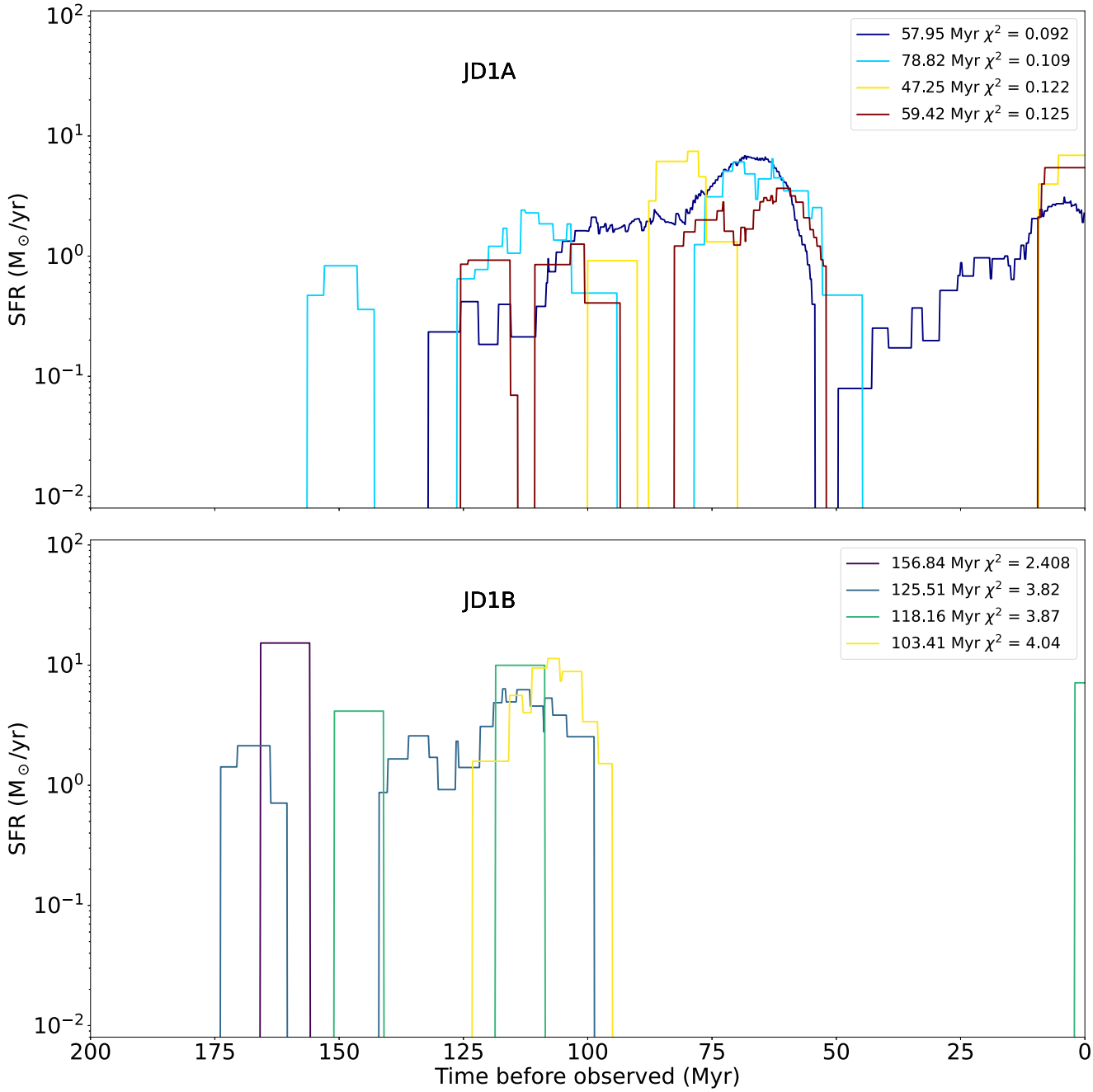

Figure 14. Star formation histories (SFHs) of simulated galaxies with colors similar to clumps A (top) and B (bottom). Note the anticorrelation: A analogs form most stars while most B analogs are less active, and vice versa. Timescales are the same on both x-axes. Mass-weighted ages and χ^2 values from SED fits are given in the legend. Photometry of the simulated galaxies was measured by Barrow et al. (2020) and matched to the observations using the GAINN deep-learning network (Santos-Olmsted et al. 2023, submitted).

surface densities $\Sigma_{\rm eff}$ are roughly on the order of ∼2000 and ∼12,000 $M_\odot$ pc^{-2}, where $\Sigma_{\rm eff} = (M/2)/(\pi R_{M/2}^2)$ and the half-mass–radius $R_{M/2} = (4/3)R_{\rm eff}$.[75] These are higher than the highest density ∼1800 $M_\odot$ pc^{-2} reported by Chen et al. (2023) because their size measurements, unaided by lensing, were only sensitive to structures with radii >150 pc. The density for clump B is just an order of magnitude less than the maximal density 10^5 $M_\odot$ pc^{-2} reported by Hopkins et al. (2010b).

A similar rough estimate of SFR densities yields ∼20 and ∼120 $M_\odot$ yr^{-1} kpc^{-2}. These are high values, though less than the highest values, >1000 $M_\odot$ yr^{-1} kpc^{-2}, reported for submillimeter galaxies.

6.5. Galaxy Clumps or Merger?

The stellar components A and B may be two merging galaxies, or they may be two clumps that formed together in situ ∼400 pc apart within a single galaxy. We cannot distinguish these scenarios with the current data. Given their masses ∼10^8 $M_\odot$, they would affect their surroundings such that we would expect them to form at the same time within a

[75] The factor of 4/3 might not be warranted since these are much larger than star clusters, in which case the densities would increase by a factor of ∼2; see Portegies Zwart et al. (2010).

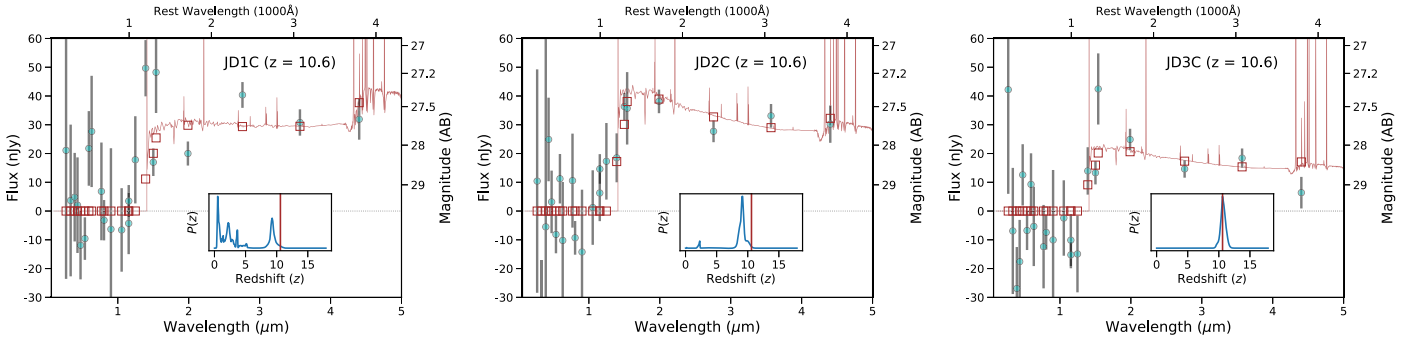

Figure 15. Candidate companion C is fainter and the photometric redshift is less clear, but its photometry can be well fit by SEDs at $z = 10.6$. EAZY SED fits are shown for JD1C, JD2C, and JD3C, left to right. Their redshift likelihood distributions $P(z)$ are shown in the insets before fixing their redshifts to $z = 10.6$ for the SED fits shown.

galaxy. A significant age difference would suggest they are separate galaxies now merging. We cannot conclusively distinguish the ages of A and B given the current data, though the simulated analog galaxies at similar redshift and SED fitting do strongly suggest their star formation to be dissimilar (see Appendix A.3).

MACS0647–JD was discovered in CLASH imaging with a search volume of a few times 1000 $\mathrm{Mpc}^3 = (10\ \mathrm{cMpc})^3$ at $z \sim 11$ (Coe et al. 2013). We employ the Astraeus cosmological simulations (Hutter et al. 2021) to calculate the likelihood of finding such a merger within that search volume. With a box size of $(230\ \mathrm{cMpc})^3$ and a minimum resolved halo mass of $M_h \sim 10^{8.6}\,M_\odot$, these simulations are ideally suited for such statistics. We find 0.176 mergers in a $(10\ \mathrm{cMpc})^3$ volume for systems such as JD1 and JD2 and 0.056 mergers per $(10\ \mathrm{cMpc})^3$ for three clumps with $M_* \sim 10^{8-9}\,M_\odot$ (Legrand et al. 2023).

Dust may also contribute to the different colors observed between A and B. Clumps are often obscured by different amounts of dust within a galaxy. Atacama Large Millimeter/submillimeter Array (ALMA) observations of $z \sim 7$ galaxies reveal spatially varying dust that is sometimes even offset from the stars observed in the rest-UV (Bowler et al. 2022; Dayal et al. 2022). JWST observations of $z \sim 6$–8 galaxies in blank fields reveal clumpy morphologies are common; each galaxy has a few multicolored star-forming complexes separated by ∼300–4300 pc, with various ages, dust reddening, and masses (Chen et al. 2023).

The ground-based spectroscopic survey VIMOS UltraDeep Survey (VUDS) found 21%–25% of $z \sim 2$–6 galaxies are dominated by two massive clumps, each $\sim 10^9$–$10^{10}\,M_\odot$, with smaller fractions of galaxies having three, four, or more clumps (Ribeiro et al. 2017). Major mergers are invoked to explain the galaxies with two massive clumps, while disk instability can explain the formation of three or more smaller clumps in situ.

6.6. A Possible Companion

The candidate companion galaxy C is also a *J*-band dropout with three lensed images at the predicted locations for a galaxy 3 kpc away at $z \sim 11$. It is >2 mag fainter, so the photometric redshifts are more uncertain. In Figure 15, we show the photometry for JD1C, JD2C, and JD3C can all be well fit with EAZY SEDs assuming $z = 10.6$. (This is also the most likely redshift for JD3C, though it is not for JD1C and JD2C.)

The redshift can also be constrained from strong-lens mass modeling. Both of our lens models (Section 3.1) find the observed lensed image locations are best fit by high-redshift solutions $z \sim 11$.

6.7. Comparisons to Simulated Galaxies

We compare our results to various expectations from large cosmological semi-analytic models, an *N*-body cosmological simulation, and high-resolution zoom-in hydrodynamic simulations of the early universe.

We first compare to the DELPHI semi-analytic model (Dayal et al. 2014, 2022). In brief, this model reconstructs galaxy halo assembly histories from $z \sim 40$–4.5, tracking buildup of gas and star formation, including feedback. With minimal free parameters and calibration, it reproduces observed high-z luminosity functions, stellar mass functions, and ALMA dust estimates. Details are provided in Appendix A.2.

Given a stellar mass of 10^8 (10^9) $M_\odot$ at $z \sim 10.6$, DELPHI predicts a host halo mass $M_h \sim 10^{10}$ (10^{11}) $M_\odot$, absolute UV magnitude $M_{\mathrm{UV}} \sim -19.5$ (−20), dust $A_V \sim 0.03$ (0.12) mag, and a stellar radius ∼70 (350) pc for galaxies at $z \sim 10$, consistent with our observations, especially for the lower-end stellar mass $10^8\,M_\odot$. Finally, this model predicts stellar mass-weighted ages that range between 35 and 180 Myr for galaxies of a similar mass at $z \sim 10$; the range of ages reflects the varied assembly histories.

These small amounts of dust are also consistent with recent modeling by Ferrara et al. (2022) suggesting that negligible dust at these redshifts could help explain the unexpectedly large numbers of $z \sim 10$–14 candidates reported in early JWST observations.

Next, we consider the merging galaxies from a hydrodynamic simulation (Barrow et al. 2017), presented in Figure 6, that bears a resemblance to MACS0647–JD A+B and C. This was the most massive halo in that simulation, and it has a total stellar mass $4 \times 10^7\,M_\odot$. The analog C is connected by a faint filament of stars and gas. This configuration was likely the result of previous galaxy mergers, including A+B, as evidenced by hot regions tracing supernova remnants.

Within a separate hydrodynamic simulation of a 66 Mpc^3 comoving volume with adaptive mesh refinement resolution sufficient to track gas down to 0.25 pc at $z = 12$ and form individual Population III stars as well as metal-enriched star clusters (Santos-Olmsted et al. 2023, submitted), we perform a more thorough search for simulated galaxies with colors similar to A and B. The best-matching analogs have mass-weighted ages of ∼50 and ∼125 Myr, with B having little or no SFR within the past 100 Myr before observation. Bursty SFHs with

dormant periods of several tens of millions of years are common in these simulations. Observationally, the question is whether we observe them when they are active with SFR in the past 10 Myr and thus brightest in the rest-UV.

JD1A's photometry was well matched to SEDs from the simulation (Santos-Olmsted et al. 2023, submitted) showing routine bursts of star formation, while JD1B showed clear evidence of suppressed star formation with a relatively flat UV slope and weaker evidence for the presence of emission lines. The close projected distance of only 400 pc in a halo that should be several kiloparsecs wide for a stellar population of this mass might imply that the two regions formed in the same halo, but the SED fits SFHs with suppressed star formation for several dynamical times in only B. The difference in SFHs implies that both halos were subject to independent radiative and dynamical environments and likely formed much farther apart than 400 pc before coming closer, or, alternatively, both objects may be farther apart than their projected separation despite their coincident redshift. Both scenarios, the SED model and the simulation, suggest an in-progress merger. This interaction merits further study with models tuned to investigate bursty star formation events and may yield more insight into high-redshift galaxy interactions and mergers.

6.8. Prospects of Future James Webb Space Telescope Observations

The physical properties of MACS0647–JD inferred by our JWST NIRCam observations indicate that future JWST spectroscopy should allow the detection of several strong emission lines, which would make it possible to improve constraints on the metallicity, gas ionization state, dust reddening, and SFH of this intriguing $z \approx 11$ system. Based on the photometric redshift, the planned JWST/NIRSpec PRISM observations extending to 5.3 μm ($\sim$4300 Å rest frame) may detect strong emission lines like [C III] λ1908, [O II] λ3727, Hγ and [Ne III] λ3869+Hζ+He I λ3889 (blended).

Other strong rest-frame optical emission lines like [O III] λ5007 and Hα will fall in the wavelength domain of JWST's Mid-Infrared Instrument (MIRI). The inferred SFR of MACS0647–JD suggests that both [O III] λ5007 and Hα may be detected with MIRI medium-resolution spectroscopy targeting JD1, which would then also allow simultaneous MIRI imaging of part of the MACS0647 cluster field. Such MIRI imaging could, depending on the position angle, also cover JD3, which is predicted to be sufficiently bright for detection in both F560W and F770W.

7. Conclusions

In this study, we report on public JWST imaging observations of the $z \sim 11$ galaxy MACS0647–JD taken with six NIRCam filters (F115W, F150W, F200W, F277W, F356W, and F444W) by GO program 1433 (PI: Coe). Three lensed images are observed with magnifications $\sim$8, 5, and 2 and F356W AB mags of 25.1, 25.6, and 26.6. The delensed F356W magnitude is 27.3, with $M_{\rm UV} = -20.4\% \pm 17\%$. MACS0647–JD is a *J*-band dropout appearing in all filters redward of F115W. Its photometric redshift is $z = 10.6 \pm 0.3$ as estimated by six different methods.

MACS0647–JD is spatially resolved into two components, A and B, separated by $\sim$400 pc in projection. They may be merging galaxies or two clumps that formed in situ within one galaxy.

Component A is brighter and very blue ($\beta \sim -2.6 \pm 0.1$), dust-free with a delensed radius $\sim 70^{+24}_{-24}$ pc, and mass-weighted age $\sim$50 Myr. Component B is smaller and redder with perhaps some dust $A_V \sim 0.1$ mag, a delensed radius $\sim 20^{+8}_{-5}$ pc, and mass-weighted age $\sim$100 Myr. Simulated galaxies with similar colors as observed for A and B at similar redshift have dissimilar SFHs despite their proximity, which is consistent with our SED-fitting results, suggesting they formed some distance apart, perhaps as separate galaxies observed now as they were on their way to merge.

Both have stellar masses $\sim 10^8\,M_\odot$, with A likely more massive by a factor of 2 or so. With SFRs on the order of 1 $M_\odot$ yr^{-1} averaged over the past 10 Myr and sSFRs $\sim$10 Gyr^{-1}, these galaxies are consistent with expectations for the stellar main sequence at $z \sim 11$. Given their small radii $<$100 pc, they have very high stellar mass surface densities, up to $\sim 10^4\,M_\odot$ pc^{-2}, with correspondingly large SFR surface densities up to $\sim 100\,M_\odot$ yr^{-1} kpc^{-2}. These are large, though not exceeding theoretical limits or values measured for other extreme objects.

A small candidate companion galaxy, C, is identified $\sim$3 kpc away. Three lensed images of C at the expected locations are all *J*-band dropouts. While fainter (F356W AB mag $\sim$ 28) with more uncertain photometry, its SED is consistent with $z \sim 10.6$.

The NIRCam imaging spans 1–5 μm to rest-frame 4300 Å at $z = 10.6$. F444W is only partially redward of the Balmer break, limiting our ability to estimate ages and stellar masses. Additional observations with the reddest NIRCam filter, F480M, and the NIRSpec MSA PRISM are upcoming and planned for 2023 January.

We are grateful and indebted to all 20,000 people who worked to make JWST an incredible discovery machine.

We dedicate these JWST observations to Rob Hawkins, former lead developer of the Astronomer's Proposal Tool (APT). Rob lost his life in 2020 November while astronomers around the world were using APT to prepare observations we proposed for JWST Cycle 1.

This work is based on observations made with the NASA/ESA/CSA James Webb Space Telescope (JWST) and Hubble Space Telescope (HST). The data were obtained from the Mikulski Archive for Space Telescopes (MAST) at the Space Telescope Science Institute (STScI), which is operated by the Association of Universities for Research in Astronomy (AURA), Inc., under NASA contract NAS 5-03127 for JWST. These observations are associated with programs JWST-GO 1433 and HST-GO 9722, 10493, 10793, and 12101.

T.H. and A. were funded by a grant for JWST-GO-01433 provided by STScI under NASA contract NAS 5-03127. L.W. acknowledges support from the National Science Foundation Graduate Research Fellowship under grant No. DGE-2137419. A.A. acknowledges support from the Swedish Research Council (Vetenskapsrådet project grant No. 2021-05559). P. D. acknowledges support from the NWO grant 016. VIDI.189.162 ("ODIN") and the European Commission's and University of Groningen's CO-FUND Rosalind Franklin program and warmly thanks the Institute for Advanced Study (IAS) Princeton, where a part of this work was carried out, for their generous hospitality and support through the Bershadsky Fund. The Cosmic Dawn Center is funded by the Danish National Research Foundation (DNRF) under grant #140. E.Z.

and A.V. ackowledge support from the Swedish National Space Agency. M.B. acknowledges support from the Slovenian national research agency ARRS through grant No. N1-0238. M.O. acknowledges support from JSPS KAKENHI grant Nos. JP22H01260, JP20H05856, JP20H00181, and JP22K21349. A. Z., A.K.M., and L.J.F. acknowledge support by grant No. 2020750 from the United States-Israel Binational Science Foundation (BSF) and grant No. 2109066 from the United States National Science Foundation (NSF), and by the Ministry of Science & Technology, Israel. E.V. and M.N. acknowledge financial support through grant Nos. PRIN-MIUR 2017WSCC32 and 2020SKSTHZ and INAF "main-stream" grant Nos. 1.05.01.86.20 and 1.05.01.86.31. Y.J.-T. acknowledges financial support from the European Union's Horizon 2020 research and innovation program under the Marie Sklodowska-Curie grant agreement No. 898633, the MSCA IF Extensions Program of the Spanish National Research Council (CSIC), and the State Agency for Research of the Spanish MCIU through the Center of Excellence Severo Ochoa award to the Instituto de Astrofísica de Andalucía (SEV-2017-0709). A.C.C. thanks the Leverhulme Trust for their support via a Leverhulme Early Career Fellowship.

Facilities: JWST(NIRCam), HST(ACS, WFC3).

Software: ASTROPY (Astropy Collaboration et al. 2013, 2018, 2022), PHOTUTILS (Bradley et al. 2022), GRIZLI (Brammer et al. 2022), EAZYPY (Brammer et al. 2008), PIXEDFIT (Abdurro'uf et al. 2021, 2022) `Bagpipes` (Carnall et al. 2018), CLOUDY(Ferland et al. 1998, 2013, 2017), Prospector (Leja et al. 2017; Johnson et al. 2021), BEAGLE (Chevallard & Charlot 2016), JDAVIZ (JDADF Developers et al. 2022).

Appendix

A.1. Photometry Measurement for Individual Clumps

In Section 4, we measure the photometry for components A and B using different methods including PIXEDFIT, IMFIT, and CHEFs. Only the photometry from PIXEDFIT was used for SED fitting to estimate physical properties. Here, we provide a comparison among the three different methods, which is shown in Figure 16. We also test the SED fitting for the photometry from IMFIT and CHEFs. The results are similar to the result using PIXEDFIT photometry.

A.2. DELPHI Semi-analytic Model

In brief, the DELPHI semi-analytic model (Dayal et al. 2014, 2022) uses a binary merger tree approach to build the dark matter assembly histories of $z \sim 4.5$ galaxies with halo masses $\log(M_h/M_\odot) = 8$–14 up to $z \sim 40$. It then jointly tracks the buildup of dark matter halos and their baryonic components (gas, stellar, metal, and dust mass) between $z \sim 40$–4.5 including the impact of both internal (supernova) and external (reionziation) feedback; here, we consider a case that ignores reionization feedback since reionization affects $\lesssim$20% of the volume of the universe at $z \sim 10.5$ (Dayal et al. 2020). The key strength of this model lies in its minimal free parameters (the star formation efficiency and fraction of supernova energy coupling to gas) and the fact that is it baselined against all available high-z data sets including the evolving UV luminosity function, the stellar mass function, and the most recent dust estimates at $z \sim 7$ from the Reionization Era Bright Emission Line Survey ALMA large program (Bouwens et al. 2022).

A.3. GAINN Analog Simulated Galaxies

Synthetic fluxes from JWST's wideband filters F115W, F150W, F200W, F277W, F356W, and F444W were used as a training set for photometric redshift predictions of the combined fluxes of the A and B objects using the GAINN method (Santos-Olmsted et al. 2023, submitted), which trains deep convolutional neural networks on synthetic photometry created in post-processing from in situ star-forming ENZO (Bryan et al. 2014) radiative-hydrodynamic simulations. GAINN was originally designed for redshifts higher than

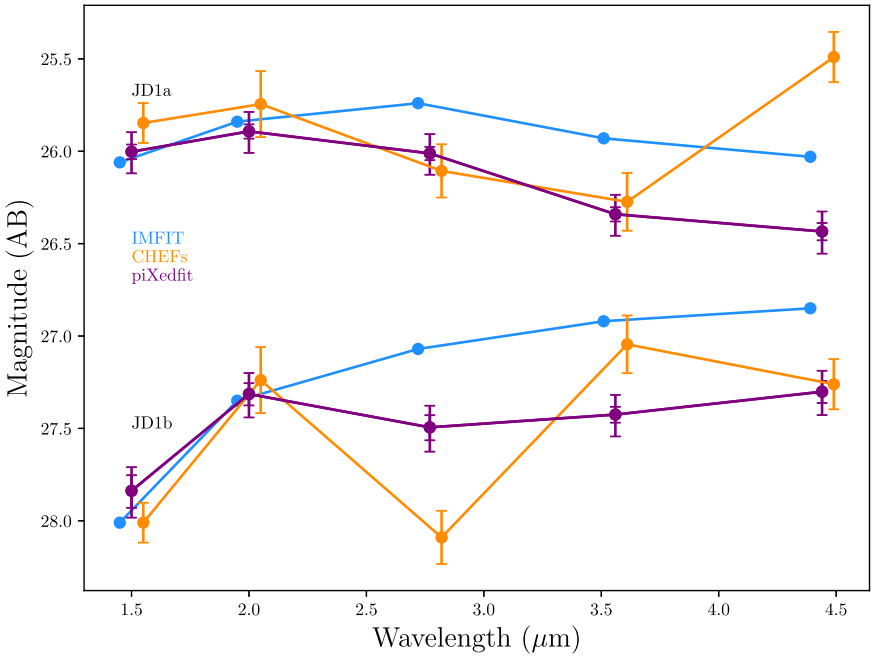

Figure 16. Photometry of JD1A and JD1B measured from three different methods, PIXEDFIT, IMFIT, and CHEFs, with 3% and 10% uncertainty added in quadrature for PIXEDFIT.

11.4, and so the SFHs were shifted forward in time by 50, 100, and 150 Myr to produce a training set. Then, a 20-layer network was trained on the approximately 12,000 SEDs in the set that fell between $z = 12$ and $z = 10$ to accommodate the likely redshift of MACS0647–JD, and achieved a mean absolute error of 0.0261 in the validation set. Predicted redshifts for MACS0647–JD were consistent with galaxies at $z \sim 10.6$, returning a value of $z = 10.6417$ for object A and a value of $z = 10.5614$ for object B.

Additionally, χ^2 SED fitting to GAINN-simulated galaxies was performed on JD1A's and JD1B's fluxes in F200W, F277W, F356W, and F444W, which focus on the rest-UV slope of both objects. Fitting was accomplished by first shifting over 10,000 synthetic observations in GAINN to $z = 10.6$ and then using relative synthetic flux to create a mass- and redshift-independent comparison. Then, the synthetic flux of the SED was scaled to the observed flux of JD1A and JD1B and χ^2 values were calculated for the other three bands. We report four SFHs corresponding to the lowest values of χ^2 for both JD1A and JD1B along with their mass-weighted mean stellar age after restricting our output to the best-fit result in any particular halo tree branch.

JD1B's spectra was relatively rare in the simulation, resulting in various predictions with higher squared error, but it often matched to SFHs with the strongest episodes of star formation ending earlier than 100 Myr before the observation, with some results showing a more recent burst. The predicted mean stellar ages were between 100 and 160 Myr, which is consistent with an absence of young stars and the flat UV slope of JD1B.

All histories matched to JD1A featured bursty episodes of star formation peaking between 50 and 100 Myr before the observation, followed by a turnoff and a resumption of star formation at the time of observation. Predictions for mean stellar age also converged between 45 and 80 Myr, which was consistent with the observed blue UV slope. All matched SEDs had strong emission lines, implying that previous episodes of star formation well enriched the ISM.

ORCID iDs

Tiger Yu-Yang Hsiao https://orcid.org/0000-0003-4512-8705
Dan Coe https://orcid.org/0000-0001-7410-7669
Abdurro'uf https://orcid.org/0000-0002-5258-8761
Lily Whitler https://orcid.org/0000-0003-1432-7744
Intae Jung https://orcid.org/0000-0003-1187-4240
Gourav Khullar https://orcid.org/0000-0002-3475-7648
Ashish Kumar Meena https://orcid.org/0000-0002-7876-4321
Pratika Dayal https://orcid.org/0000-0001-8460-1564
Kirk S. S. Barrow https://orcid.org/0000-0002-8638-1697
Lillian Santos-Olmsted https://orcid.org/0000-0002-8763-3702
Adam Casselman https://orcid.org/0000-0001-9055-7045
Eros Vanzella https://orcid.org/0000-0002-5057-135X
Mario Nonino https://orcid.org/0000-0001-6342-9662
Yolanda Jiménez-Teja https://orcid.org/0000-0002-6090-2853
Masamune Oguri https://orcid.org/0000-0003-3484-399X
Lukas J. Furtak https://orcid.org/0000-0001-6278-032X
Adi Zitrin https://orcid.org/0000-0002-0350-4488
Angela Adamo https://orcid.org/0000-0002-8192-8091
Gabriel Brammer https://orcid.org/0000-0003-2680-005X
Larry Bradley https://orcid.org/0000-0002-7908-9284
Jose M. Diego https://orcid.org/0000-0001-9065-3926
Erik Zackrisson https://orcid.org/0000-0003-1096-2636
Steven L. Finkelstein https://orcid.org/0000-0001-8519-1130
Rogier A. Windhorst https://orcid.org/0000-0001-8156-6281
Rachana Bhatawdekar https://orcid.org/0000-0003-0883-2226
Taylor A. Hutchison https://orcid.org/0000-0001-6251-4988
Tom Broadhurst https://orcid.org/0000-0002-8785-8979
Paola Dimauro https://orcid.org/0000-0001-7399-2854
Felipe Andrade-Santos https://orcid.org/0000-0002-8144-9285
Jan J. Eldridge https://orcid.org/0000-0002-1722-6343
Ana Acebron https://orcid.org/0000-0003-3108-9039
Roberto J. Avila https://orcid.org/0000-0001-9364-5577
Matthew B. Bayliss https://orcid.org/0000-0003-1074-4807
Alex Benítez https://orcid.org/0000-0002-0705-3178
Christian Binggeli https://orcid.org/0000-0002-0808-4136
Patricia Bolan https://orcid.org/0000-0002-7365-4131
Maruša Bradač https://orcid.org/0000-0001-5984-0395
Adam C. Carnall https://orcid.org/0000-0002-1482-5818
Christopher J. Conselice https://orcid.org/0000-0003-1949-7638
Megan Donahue https://orcid.org/0000-0002-2808-0853
Brenda Frye https://orcid.org/0000-0003-1625-8009
Seiji Fujimoto https://orcid.org/0000-0001-7201-5066
Alaina Henry https://orcid.org/0000-0002-6586-4446
Bethan L. James https://orcid.org/0000-0003-4372-2006
Susan A. Kassin https://orcid.org/0000-0002-3838-8093
Lisa Kewley https://orcid.org/0000-0001-8152-3943
Rebecca L. Larson https://orcid.org/0000-0003-2366-8858
Tod Lauer https://orcid.org/0000-0003-3234-7247
David Law https://orcid.org/0000-0002-9402-186X
Guillaume Mahler https://orcid.org/0000-0003-3266-2001
Ramesh Mainali https://orcid.org/0000-0003-0094-6827
Stephan McCandliss https://orcid.org/0000-0003-0503-4667
David Nicholls https://orcid.org/0000-0003-0892-5203
Norbert Pirzkal https://orcid.org/0000-0003-3382-5941
Marc Postman https://orcid.org/0000-0002-9365-7989
Jane R. Rigby https://orcid.org/0000-0002-7627-6551
Russell Ryan https://orcid.org/0000-0003-0894-1588
Peter Senchyna https://orcid.org/0000-0002-9132-6561
Keren Sharon https://orcid.org/0000-0002-7559-0864
Victoria Strait https://orcid.org/0000-0002-6338-7295
Mengtao Tang https://orcid.org/0000-0001-5940-338X
Michele Trenti https://orcid.org/0000-0001-9391-305X
Anton Vikaeus https://orcid.org/0000-0002-4853-1076
Brian Welch https://orcid.org/0000-0003-1815-0114

References

Abdurro'uf, Lin, Y.-T., Wu, P.-F., & Akiyama, M. 2021, ApJS, 254, 15
Abdurro'uf, Lin, Y.-T., Wu, P.-F., & Akiyama, M. 2022, piXedfit: Analyze Spatially Resolved SEDs of Galaxies, Astrophysics Source Code Library, ascl:2207.033
Abdurro'uf, Coe, D., Jung, I., et al. 2023, ApJ, 945, 117
Adams, N. J., Conselice, C. J., Ferreira, L., et al. 2022, MNRAS, 518, 4755
Astropy Collaboration, Price-Whelan, A. M., Lim, P. L., et al. 2022, ApJ, 935, 167

Astropy Collaboration, Price-Whelan, A. M., Sipőcz, B. M., et al. 2018, AJ, 156, 123
Astropy Collaboration, Robitaille, T. P., Tollerud, E. J., et al. 2013, A&A, 558, A33
Atek, H., Shuntov, M., Furtak, L. J., et al. 2023, MNRAS, 519, 1201
Averbukh, J., Bradley, L., et al. 2022, JDADF DevelopersJdaviz, v2.10.0, Zenodo, doi:10.5281/zenodo.5513927
Barbary, K. 2016, JOSS, 1, 58
Barnes, J. E. 1992, ApJ, 393, 484
Barrow, K. S. S., Robertson, B. E., Ellis, R. S., et al. 2020, ApJL, 902, L39
Barrow, K. S. S., Wise, J. H., Norman, M. L., O'Shea, B. W., & Xu, H. 2017, MNRAS, 469, 4863
Behroozi, P., Wechsler, R. H., Hearin, A. P., & Conroy, C. 2019, MNRAS, 488, 3143
Bell, E. F., Phleps, S., Somerville, R. S., et al. 2006, ApJ, 652, 270
Belokurov, V., Erkal, D., Evans, N. W., Koposov, S. E., & Deason, A. J. 2018, MNRAS, 478, 611
Bertin, E., & Arnouts, S. 1996, A&AS, 117, 393
Bonaca, A., Conroy, C., Cargile, P. A., et al. 2020, ApJL, 897, L18
Bouwens, R. J., Bradley, L., Zitrin, A., et al. 2014, ApJ, 795, 126
Bouwens, R. J., Smit, R., Schouws, S., et al. 2022, ApJ, 931, 160
Bowler, R. A. A., Cullen, F., McLure, R. J., Dunlop, J. S., & Avison, A. 2022, MNRAS, 510, 5088
Bradley, L. D., Coe, D., Brammer, G., et al. 2022, arXiv:2210.01777
Bradley, L. D., Zitrin, A., Coe, D., et al. 2014, ApJ, 792, 76
Brammer, G., Strait, V., Matharu, J., & Momcheva, I. 2022, grizli, v1.5.0, Zenodo, doi:10.5281/zenodo.6672538
Brammer, G. B., van Dokkum, P. G., & Coppi, P. 2008, ApJ, 686, 1503
Brammer, G. B., van Dokkum, P. G., Illingworth, G. D., et al. 2013, ApJL, 765, L2
Broadhurst, T., Benítez, N., Coe, D., et al. 2005, ApJ, 621, 53
Bryan, G. L., Norman, M. L., O'Shea, B. W., et al. 2014, ApJS, 211, 19
Burke, C., Hilton, M., & Collins, C. 2015, MNRAS, 449, 2353
Carnall, A. C., McLure, R. J., Dunlop, J. S., & Dave, R. 2018, MNRAS, 480, 4379
Castellano, M., Fontana, A., Treu, T., et al. 2022, ApJL, 938, L15
Chabrier, G. 2003, PASP, 115, 763
Chan, B. M. Y., Broadhurst, T., Lim, J., et al. 2017, ApJ, 835, 44
Charlot, S., & Fall, S. M. 2000, ApJ, 539, 718
Chen, Z., Stark, D. P., Endsley, R., et al. 2023, MNRAS, 518, 5607
Chevallard, J., & Charlot, S. 2016, MNRAS, 462, 1415
Claeyssens, A., Adamo, A., Richard, J., et al. 2023, MNRAS, 520, 2180
Coe, D., Salmon, B., Bradac, M., et al. 2019, ApJ, 884, 85
Coe, D., Umetsu, K., Zitrin, A., et al. 2012, ApJ, 757, 22
Coe, D., Zitrin, A., Carrasco, M., et al. 2013, ApJ, 762, 32
Connor, T., Donahue, M., Kelson, D. D., et al. 2017, ApJ, 848, 37
Conroy, C., Gunn, J. E., & White, M. 2009, ApJ, 699, 486
Dayal, P., Ferrara, A., Dunlop, J. S., & Pacucci, F. 2014, MNRAS, 445, 2545
Dayal, P., Ferrara, A., Sommovigo, L., et al. 2022, MNRAS, 512, 989
Dayal, P., Volonteri, M., Choudhury, T. R., et al. 2020, MNRAS, 495, 3065
Dekel, A., Birnboim, Y., Engel, G., et al. 2009, Natur, 457, 451
Dekel, A., Zolotov, A., Tweed, D., et al. 2013, MNRAS, 435, 999
Di Cesare, C., Graziani, L., Schneider, R., et al. 2023, MNRAS, 519, 4632
Diego, J. M., Protopapas, P., Sandvik, H. B., & Tegmark, M. 2005, MNRAS, 360, 477
Diego, J. M., Tegmark, M., Protopapas, P., & Sandvik, H. B. 2007, MNRAS, 375, 958
Donahue, M., Connor, T., Fogarty, K., et al. 2015, ApJ, 805, 177
Donnan, C. T., McLeod, D. J., Dunlop, J. S., et al. 2023, MNRAS, 518, 6011
Duncan, K., Conselice, C. J., Mundy, C., et al. 2019, ApJ, 876, 110
Ebeling, H., Barrett, E., Donovan, D., et al. 2007, ApJL, 661, L33
Eichner, T., Seitz, S., Suyu, S. H., et al. 2013, ApJ, 774, 124
Eldridge, J. J. 2020, A&G, 61, 2.24
Eldridge, J. J., & Stanway, E. R. 2009, MNRAS, 400, 1019
Eldridge, J. J., & Stanway, E. R. 2022, ARA&A, 60, 455
Ellison, S. L., Viswanathan, A., Patton, D. R., et al. 2019, MNRAS, 487, 2491
Erwin, P. 2015, ApJ, 799, 226
Falcón-Barroso, J., Sánchez-Blázquez, P., Vazdekis, A., et al. 2011, A&A, 532, A95
Ferland, G. J., Chatzikos, M., Guzmán, F., et al. 2017, RMxAA, 53, 385
Ferland, G. J., Korista, K. T., Verner, D. A., et al. 1998, PASP, 110, 761
Ferland, G. J., Porter, R. L., van Hoof, P. A. M., et al. 2013, RMxAA, 49, 137
Feroz, F., & Hobson, M. P. 2008, MNRAS, 384, 449
Feroz, F., Hobson, M. P., & Bridges, M. 2009, MNRAS, 398, 1601
Feroz, F., & Skilling, J. 2013, in AIP Conf. Ser. 1553, Bayesian Inference and Maximum Entropy Methods in Science and Engineering: 32nd Int. Workshop on Bayesian Inference and Maximum Entropy Methods in Science and Engineering, ed. U. von Toussaint (Melville, NY: AIP), 106
Ferrara, A., Pallottini, A., & Dayal, P. 2022, arXiv:2208.00720
Ferreira, L., Adams, N., Conselice, C. J., et al. 2022, ApJ, 938, L2
Finkelstein, S. L., Bagley, M. B., Arrabal Haro, P., et al. 2022, ApJ, 940, L55
Fogarty, K., Postman, M., Larson, R., Donahue, M., & Moustakas, J. 2017, ApJ, 846, 103
Furtak, L. J., Shuntov, M., Atek, H., et al. 2023, MNRAS, 519, 3064
Gaia Collaboration, Brown, A. G. A., Vallenari, A., et al. 2021, A&A, 649, A1
Gardner, J. P., Mather, J. C., Clampin, M., et al. 2006, SSRv, 123, 485
Girardi, L., Bressan, A., Bertelli, G., & Chiosi, C. 2000, A&AS, 141, 371
Gómez-Valent, A., & Amendola, L. 2018, JCAP, 2018, 051
Graur, O., Rodney, S. A., Maoz, D., et al. 2014, ApJ, 783, 28
Gutkin, J., Charlot, S., & Bruzual, G. 2016, MNRAS, 462, 1757
Harikane, Y., Ouchi, M., Oguri, M., et al. 2023, ApJS, 265, 5
Helmi, A., Babusiaux, C., Koppelman, H. H., et al. 2018, Natur, 563, 85
Hoffmann, S. L., Mack, J., Avila, R., et al. 2021, BAAS, 53, 2021n6i216p02
Hopkins, P. F., Bundy, K., Croton, D., et al. 2010a, ApJ, 715, 202
Hopkins, P. F., Murray, N., Quataert, E., & Thompson, T. A. 2010b, MNRAS, 401, L19
Husko, F., Lacey, C. G., & Baugh, C. M. 2023, MNRAS, 518, 5323
Hutter, A., Dayal, P., Yepes, G., et al. 2021, MNRAS, 503, 3698
Inoue, A. K., Shimizu, I., Iwata, I., & Tanaka, M. 2014, MNRAS, 442, 1805
Jiménez-Teja, Y., & Benítez, N. 2012, ApJ, 745, 150
Johnson, B. D., Leja, J., Conroy, C., & Speagle, J. S. 2021, ApJS, 254, 22
Jullo, E., & Kneib, J.-P. 2009, MNRAS, 395, 1319
Jullo, E., Kneib, J.-P., Limousin, M., et al. 2007, NJPh, 9, 447
Khusanova, Y., Bethermin, M., Le Fèvre, O., et al. 2021, A&A, 649, A152
Koekemoer, A. M., Fruchter, A. S., Hook, R. N., & Hack, W. 2003, in HST Calibration Workshop: Hubble after the Installation of the ACS and the NICMOS Cooling System, ed. S. Santiago, A. Koekemoer, & B. Whitmore (Baltimore, MD: Space Telescope Science Institute), 337
Kroupa, P. 2002, Sci, 295, 82
Kroupa, P., Tout, C. A., & Gilmore, G. 1993, MNRAS, 262, 545
Lam, D., Bouwens, R. J., Coe, D., et al. 2019, arXiv:1903.08177
Leethochawalit, N., Trenti, M., Santini, P., et al. 2023, ApJ, 942, L26
Legrand, L., Dayal, P., Hutter, A., et al. 2023, MNRAS, 519, 4564
Leja, J., Carnall, A. C., Johnson, B. D., Conroy, C., & Speagle, J. S. 2019, ApJ, 876, 3
Leja, J., Johnson, B. D., Conroy, C., van Dokkum, P. G., & Byler, N. 2017, ApJ, 837, 170
Lotz, J. M., Jonsson, P., Cox, T. J., et al. 2011, ApJ, 742, 103
Lotz, J. M., Koekemoer, A., Coe, D., et al. 2017, ApJ, 837, 97
Madau, P., & Dickinson, M. 2014, ARA&A, 52, 415
Marigo, P., & Girardi, L. 2007, A&A, 469, 239
Marigo, P., Girardi, L., Bressan, A., et al. 2008, A&A, 482, 883
Meneghetti, M., Natarajan, P., Coe, D., et al. 2017, MNRAS, 472, 3177
Merten, J., Meneghetti, M., Postman, M., et al. 2015, ApJ, 806, 4
Meštrić, U., Vanzella, E., Zanella, A., et al. 2022, MNRAS, 516, 3532
Mihos, J. C., & Hernquist, L. 1996, ApJ, 464, 641
Naab, T., Johansson, P. H., & Ostriker, J. P. 2009, ApJL, 699, L178
Naidu, R. P., Conroy, C., Bonaca, A., et al. 2021, ApJ, 923, 92
Naidu, R. P., Oesch, P. A., van Dokkum, P., et al. 2022, ApJ, 940, L14
Nelson, E. J., Suess, K. A., Bezanson, R., et al. 2022, arXiv:2208.01630
Newman, A. B., Ellis, R. S., Bundy, K., & Treu, T. 2012, ApJ, 746, 162
Oesch, P. A., Brammer, G., Dokkum, P. G. v., et al. 2016, ApJ, 819, 129
Oguri, M. 2010, PASJ, 62, 1017
Oke, J. B. 1974, ApJS, 27, 21
Oke, J. B., & Gunn, J. E. 1983, ApJ, 266, 713
Pacucci, F., Mesinger, A., & Haiman, Z. 2013, MNRAS, 435, L53
Pascale, M., Frye, B. L., Diego, J., et al. 2022, ApJL, 938, L6
Patel, B., McCully, C., Jha, S. W., et al. 2014, ApJ, 786, 9
Pei, Y. C. 1992, ApJ, 395, 130
Peng, C. Y., Ho, L. C., Impey, C. D., & Rix, H.-W. 2010, AJ, 139, 2097
Pirzkal, N., Coe, D., Frye, B. L., et al. 2015, ApJ, 804, 11
Planck Collaboration, Aghanim, N., Akrami, Y., et al. 2020, A&A, 641, A6
Portegies Zwart, S. F., McMillan, S. L. W., & Gieles, M. 2010, ARA&A, 48, 431
Postman, M., Coe, D., Benítez, N., et al. 2012a, ApJS, 199, 25
Postman, M., Lauer, T. R., Donahue, M., et al. 2012b, ApJ, 756, 159
Ribeiro, B., Le Fevre, O., Cassata, P., et al. 2017, A&A, 608, A16
Riess, A. G., Rodney, S. A., Scolnic, D. M., et al. 2018, ApJ, 853, 126
Rigby, J., Perrin, M., McElwain, M., et al. 2023, PASP, 135, 048001
Robitaille, T., Deil, C., & Ginsburg, A. 2020, reproject: Python-based Astronomical Image Reprojection, Astrophysics Source Code Library, ascl:2011.023

Rodney, S. A., Riess, A. G., Strolger, L.-G., et al. 2014, AJ, 148, 13
Rodriguez-Gomez, V., Genel, S., Vogelsberger, M., et al. 2015, MNRAS, 449, 49
Salim, S., Boquien, M., & Lee, J. C. 2018, ApJ, 859, 11
Sanchez-Blazquez, P., Peletier, R. F., Jimenez-Vicente, J., et al. 2006, MNRAS, 371, 703
Santos-Olmsted, L., Barrow, K., Hartwig, T., et al. 2023, arXiv:2305.17158
Sartoris, B., Biviano, A., Rosati, P., et al. 2014, ApJL, 783, L11
Smit, R., Bouwens, R. J., Labbe, I., et al. 2014, ApJ, 784, 58
Sotillo-Ramos, D., Pillepich, A., Donnari, M., et al. 2022, MNRAS, 516, 5404
Stefanon, M., Bouwens, R. J., Labbé, I., et al. 2023, ApJ, 943, 81
Stewart, K. R., Bullock, J. S., Barton, E. J., & Wechsler, R. H. 2009, ApJ, 702, 1005
Strolger, L.-G., Dahlen, T., Rodney, S. A., et al. 2015, ApJ, 813, 93
Tacchella, S., Bose, S., Conroy, C., Eisenstein, D. J., & Johnson, B. D. 2018, ApJ, 868, 92
Tacchella, S., Finkelstein, S. L., Bagley, M., et al. 2022, ApJ, 927, 170
Tasca, L. A. M., Le Fevre, O., Hathi, N. P., et al. 2015, A&A, 581, A54
Toomre, A., & Toomre, J. 1972, ApJ, 178, 623
Topping, M. W., Stark, D. P., Endsley, R., et al. 2022, MNRAS, 516, 975
Treister, E., Schawinski, K., Urry, C. M., & Simmons, B. D. 2012, ApJL, 758, L39
Umetsu, K., Medezinski, E., Nonino, M., et al. 2014, ApJ, 795, 163
van Dokkum, P. G., Whitaker, K. E., Brammer, G., et al. 2010, ApJ, 709, 1018
Vanzella, E., Castellano, M., Bergamini, P., et al. 2022, A&A, 659, A2
Welch, B., Coe, D., Zackrisson, E., et al. 2023, ApJ, 943, 2
Welch, B., Coe, D., Zitrin, A., et al. 2022, ApJL, 940, L1
Whitaker, K. E., Franx, M., Leja, J., et al. 2014, ApJ, 795, 104
Whitler, L., Endsley, R., Stark, D. P., et al. 2023a, MNRAS, 519, 157
Whitler, L., Stark, D. P., Endsley, R., et al. 2023b, MNRAS, 519, 5859
Xiang, M., & Rix, H.-W. 2022, Natur, 603, 599
Yan, H., Ma, Z., Ling, C., et al. 2023, ApJL, 942, L9
Yung, L. Y. A., Somerville, R. S., Popping, G., et al. 2019, MNRAS, 490, 2855
Zhang, H., Behroozi, P., Volonteri, M., et al. 2023, MNRAS, 518, 2123
Zheng, W., Postman, M., Zitrin, A., et al. 2012, Natur, 489, 406
Zitrin, A., Broadhurst, T., Barkana, R., Rephaeli, Y., & Benítez, N. 2011, MNRAS, 410, 1939
Zitrin, A., Broadhurst, T., Umetsu, K., et al. 2009, MNRAS, 396, 1985
Zitrin, A., Fabris, A., Merten, J., et al. 2015, ApJ, 801, 44